Summer 7-15-2017

A Thermodynamic Study of Binary Real Gas Mixtures Undergoing Normal Shocks

Josiah M. Bigelow
University of New Mexico

Josiah Michael Bigelow

Candidate

Mechanical Engineering

Department

This thesis is approved, and it is acceptable in quality and form for publication:

Approved by the Thesis Committee:

Dr. C. Randall Truman, Chairperson

Dr. Peter Vorobieff

Dr. Timothy Clark

Dr. Humberto Silva III

A Thermodynamic Study of Binary Real Gas Mixtures Undergoing Normal Shocks

by

Josiah Michael Bigelow

B.S., Mechanical Engineering, Kansas State University, 2013

THESIS

Submitted in Partial Fulfillment of the
Requirements for the Degree of

Master of Science
Mechanical Engineering

The University of New Mexico

Albuquerque, New Mexico

July, 2017

Dedication

To my wife, for her perseverance, fellowship, proof reading, and encouragement throughout this process.

"Not all who wander are lost." – Bilbo Baggins

Acknowledgments

As with any undertaking of appreciable scale and effort, the limits of who to thank are not sharply defined. I would like to take a few lines and express my gratitude, by name, to some of the most important people who have supported this project[1]. My adviser, Dr. Truman, has been truly helpful and patient throughout this project, thank you for taking me on and for all of the guidance. The members of my committee, Dr. Silva, Dr. Clark, and Dr. Vorobieff, have all provided insight into numerical modeling, fun discussions, philosophical inquiry, and humorous stories about their experiences, thank you all. A special thanks to Dr. Silva for coadvising the numerical analysis of this research. The time given by Dr. Michael Hobbs of Sandia National Laboratories in teach me how to use the TIGER code set is deeply appreciated. Dr. David Kitell, also of Sandia, provided moral support and explained how CTH worked, thank you sir! My wife, Shannon, has been a source of encouragement and support, as well as a patient listener while I describe how my programs work, thank you, and congratulations on completing your masters degree as well. My family has been not only supportive, but understanding that life is crazy when you live far away and work while going to graduate school, I love you all. I would like to thank my current and past managers at Sandia National Laboratories who have supported my continued education, Rich Graham, Abe Sego, Heather Schriner, and Nick Dereu, you all have been wonderful. Finally, I would like to thank my colleagues at Sandia who have supported and encouraged me while I have been in school, you have made the process of finishing much more enjoyable.

[1] A hearty shout out to Donald Knuth for inventing TEX

A Thermodynamic Study of Binary Real Gas Mixtures Undergoing Normal Shocks

by

Josiah Michael Bigelow

B.S., Mechanical Engineering, Kansas State University, 2013
M.S., Mechanical Engineering, University of New Mexico, 2017

Abstract

We investigate the difference between Amagat and Dalton mixing laws for gaseous equations of state (EOS) using planar traveling shocks. Numerical modeling was performed in the Sandia National Laboratories hydrocode CTH utilizing tabular EOS in the SESAME format. Numerical results were compared to experimental work from the University of New Mexico Shock Tube Laboratory. Latin hypercube samples were used to assess model sensitivities to Amagat and Dalton EOS. We find that the Amagat mixing law agrees best with the experimental results and that significant difference exist between the predictions of the Amagat and Dalton mixing methods.

Contents

List of Figures

List of Tables

Glossary

A	JWL fit parameter
α	BKW fit parameter
ASCII	American Standard Code for Information Interchange
B	JWL fit parameter
β	BKW fit parameter
BCAT	Bearcat, CTH EOS interrogation subroutine
BKW	Becker-Kistiakowsky-Wilson (equation of state)
C_{ovl}	Coefficient of overlap
χ	LHS perturbation parameter
CTH	Shock physics hydrocode
δ	Absolute relative error, percent error
DAKOTA	Design Analysis Kit for Optimization and Terascale Applications
e	Specific energy
ε	Error

Glossary

EOS	Equation of State
ID	Inner Diameter
JCZ	Jacobs-Cowperthwaite-Zwisler (equation of state)
JCZS	Jacobs-Cowperthwaite-Zwisler-Sandia (equation of state)
JWL	Jones-Wilkins-Lee (equation of state)
k	Co-volume of a gaseous component
κ	BKW fit parameter
LANL	Los Alamos National Laboratory
LJ	Lennard-Jones
LHS	Latin hypercube sample
M	Molecular mass
m	Mass
n	Mole number
ω	JWL fit parameter
P	Pressure
QoI	Quantity of Interest
R	Universal gas constant
r	Correlation coefficient or mesh refinement rate
R_g	Specific gas constant

Glossary

R_i	JWL fit parameter
ρ	Density
S	Entropy
s	Specific entropy
SNL	Sandia National Laboratories
SESAME	Tabular Equation of State
T	Temperature
θ	BKW fit parameter
U	Internal energy
UNM	University of New Mexico
V	Volume, or BKW volume ratio
v	Specific volume
V_g	Molar volume
w	Mass fraction
X	State variable
x	Mole fraction
z	Compressibility Factor

Chapter 1

Introduction and Theory

1.1 Problem Statement

The problem of how to model mixtures of real gases presents the question of which of the three measurable properties, pressure (P), temperature (T), and volume (V), apply to the whole mixture. Often the assumption is made that the measured temperature applies to the mixture leaving P and V as the variables that are a function of the components [3]. We know that for a pure, real gas the following relationship holds [4]

$$PV = mR_gTz, \tag{1.1}$$

where $z = z(P, T)$ is the compressibility factor of the gas, m is the mass, and R_g is the specific gas constant. From Amagat, we know that

$$V = \sum_{i=1}^{N} V_i, \tag{1.2}$$

where V_i is the volume occupied by component i at the given temperature and pressure of the mixture, otherwise known as the partial volume relation [3]. On the

other hand, from Dalton we find that

$$P = \sum_{i=1}^{N} P_i, \tag{1.3}$$

where P_i is the pressure exerted by the i^{th} component at the given temperature and volume of the mixture, or the partial pressure relation [3].

The following question arises when comparing binary mixtures of gases: what model is most accurate at predicting the thermodynamic properties of the mixture at a given temperature and pressure? Numerous papers have been published about multi-phase and multi-component flows [5], reacting flows, flows with arbitrary equations of state [6], and mixtures at relatively low pressures [7]. Furthermore, papers have been published on the behavior of the shock region using Monte Carlo methods in binary gas mixtures and binary gas mixtures of perfect gases [8, 9]. There are also some papers on mixtures of real gases [10, 11]. However, there is very little available on which model (Amagat or Dalton) best applies to the case of a mixture of non-reacting, real gases, undergoing shock conditions. One may assume from the context of the available material that Amagat's Law would be the natural choice but it is not entirely clear that this is true [3, 4, 5, 1]. Furthermore, both models are approximations and themselves have pressure and temperature ranges over which they may be considered accurate [3].

The aforementioned data and references indicate that there has not been much research into the specific question of mixtures of real gases under shock conditions. This raises the following questions:

a. What thermodynamic model best describes a mixture of binary real gases undergoing shocks?

b. How sensitive are the mathematical models and their numerical analogues to perturbation?

Shock waves are present in many engineering applications ranging from pneumatic systems to detonation of high explosives [1, 12]. On this spectrum applications range from fluid-particle transport to supersonic flight of spacecraft that experience atmospheric reentry. Often, the experiments needed to study a full system are cost prohibitive, time consuming, or both. One way to select a design path is to numerically model the system with appropriate boundary conditions. However, the problem of closure to the governing equations (mass, momentum, and energy) requires good representations of material properties. This is where a shock tube can provide value. The thermodynamic properties of a gas or gases can be studied under carefully controlled shock states allowing for first principles or semi-empirical models to be refined. Methods of converting a problem to a numerical representation are the 'other side of the coin' so to speak. This is where the question of how mixing is handled when using anything other than a pure gas comes in. Does the formula used to predict mixture behavior matter numerically? How can one build an accurate validation space for the numerical method employed? If one were to model a set of shocks that were impossible to reproduce in an available shock tube, how would one have confidence in the numerical answers calculated? These and other questions led to the genesis of this thesis. Not every question will be fully answered, but at the core the question of mixing will be addressed.

The following problem statement is proposed to begin to attempt to answer the questions posed above:

Model mixtures of He and SF_6 in a shock tube configuration using the Sandia National Laboratories (SNL) hydrocode CTH, utilizing SESAME table equations of state to model Amagat, Dalton, and real behaviors. Investigate model sensitivities to numerical methods, data uncertainty, modeling assumptions, and mixing ratios. Where possible, match the CTH predictions to existing experimental data.

This statement of the problem will explore the relationship of the outputs of the code

to the inputs in a rigorous and systematic way. Verification of the outputs against experimental data will provide a means to assess whether the choice of mixing model matters.

1.2 Equation of State

Equations of state (EOS) are used for closure of the system of thermodynamic equations describing a process. Conservation of mass, balance of momentum, and conservation of energy require a relationship that describes the thermodynamics of what are called state variables. Often the state variables used are ones that are easily measured experimentally such as P, T, and V. However, this need not always be the case, because one could also construct an equation of state in terms of variables like entropy, S, and internal energy, U, which are impossible to directly measure experimentally [13]. Equations of state are difficult to construct entirely from first principles with the constraint that they also be perfectly accurate for all physical phases of a material. The ideal gas equation is an example of one such equation that works well at describing the nature of many different gases, provided the density is not too high. For example, if the modeled gas begins to condense the latent heat of vaporization and the change in density from compressible to incompressible fluid are not captured in the ideal gas model. In engineering modeling, equations of state are often curve fits to experimental data that are semi-empirical in nature. Parts of the equation of state are known from fundamental physics and other parts are "fit" to improve the results of the equation(s) over a particular range of states [4, 13]. For this problem EOS selection considered gaseous states of Helium (He) and SF_6 in a shock region since phase change was not part of the problem.

1.3 Numerical Analysis

Shock modeling is inherently difficult in a numerical sense [14]. Great care is required to make codes stable and accurate across the shock since a shock is often represented as a discontinuous jump state, introducing a cusp into the numerical results often leading to numerical instability [14]. This research is interested in differences that may be present in mixing formulations but not what is happening inside of the shock. The primary interest is in the effect of the shock front as it passes through the gas mixture. Any numerical algorithm utilized need only accurately represent the shock effects, e.g., shock speed, shock pressure, and shock temperature, but does not need to provide an accurate representation of the shock width or interior structure.

1.4 Verification and Validation

Verification and validation are distinct and important aspects of any numerical analysis. Verification can be thought of as checking that the correct physical models or theories were applied. Have the governing equations been satisfied, was the mathematical analysis performed correctly? Verification is an objective measure since there are clear correct and incorrect applications of a physical law or principle. However, validation is harder to achieve. Assumptions, numerical error, algorithm choice, etc. all play into the validity of observed numerical results. Validation requires carefully analyzing the process and also performing studies on model sensitivity. Generating a validation space requires objective as well as subjective judgment about mesh refinement, statistics, and numerical methods. For this research, verification takes the form of using codes that are known to provide good shock state results and accurately model EOS. Rankine-Hugoniot analysis provided certainty that EOS surfaces passed through the correct thermodynamic states. Validation came through comparison to

experimental values and exercising models via Latin hypercube sampling.

Chapter 2

Methodology

2.1 Equation of State

Numerical analogues to an analytic EOS were implemented in the form of SESAME tables. This section discusses EOS engineering models considered, selection criteria, and mixture table creation.

2.1.1 EOS Model

Four different equation of state models were considered for this research, and are in ascending order of complexity, Ideal Gas [15], Becker-Kistiakowsky-Wilson (BKW) [16], Jones-Wilkins-Lee (JWL) [17, 18], and Jacobs-Cowperthwaite-Zwisler (JCZ) [19, 20]. The Ideal Gas model has promise for relatively weak shocks since the density does not get very large. However, the stronger the shock, the worse the Ideal Gas model will perform. The ideal gas, JWL, and BKW models were discarded after some consideration due to questions regarding accuracy and the fact that they have been superseded by the JCZ equations of state [20].

The ideal gas law was first proposed in 1834 by Emile Clapeyron in an article published by the Ècole Polytechnique in Paris, France [15]. A common formulation is

$$PV = mR_gT, \tag{2.1}$$

where variable definitions have not changed from Equation 1.1. The drawback of the Ideal Gas law is that if the density of the gas gets too large (either liquification or under high compression) the model breaks down. Furthermore, Amagat and Dalton formulations reduce to the same representation in an ideal gas [3].

The BKW equations are based on a co-volume model

$$\frac{PV_g}{RT} = 1 + Xe^{\beta X}, \qquad X = \frac{\kappa \sum x_i k_i}{V_g(T+\theta)^\alpha}, \tag{2.2}$$

where P is the pressure, V_g the molar volume, and T the temperature of the gas. Furthermore, R is the universal gas constant, e is Euler's number, β, κ, k_i, θ, and α are empirically determined constants, and x_i is the mole fraction of the i^{th} component [16]. The principal drawback of the BKW equations is that one needs to calibrate the fit for every new material modeled leading to considerable variance in fitted parameter values [21]. One advantage of the BKW EOS is that it is completely analytic. Having a closed form analytic model allows for fast calculation of thermodynamic states. However, the question remains whether the fit is any good, given the large number of parameters to adjust.

The JWL EOS is

$$P = A\left(1 - \frac{\omega}{R_1V}\right)e^{-R_1V} + B\left(1 - \frac{\omega}{R_2V}\right)e^{-R_2V} + \frac{\omega\rho_e e}{V}, \tag{2.3}$$

where P is the pressure, V is the volume ratio of the explosive to detonation products, and e is the internal energy [17]. The JWL parameters are A, B, R_1, R_2, and ω, which are tuned to a specific material [18]. Since our research does not involve explosives, this particular EOS is a poor choice. SNL codes do have implementations

of JWL, but this EOS is particularly tuned to solid explosives that burn to produce gaseous and condensed products [22]. The properties predicted are predicated on line integrals along adiabatic expansion paths from an initial high temperature and pressure state, and so would not necessarily be suited to a room temperature starting condition [22].

The Jacobs-Cowperthwaite-Zwisler (JCZ) EOS was originally developed to give a more general representation over a wide range of material densities [19]. SNL updated the original TIGER [19] code and JCZ EOS with improved fits over ionization ranges and additional molecular species in what is now called the JCZS EOS [12, 20]. Originally, JCZ variants were denoted by a number (e.g., JCZ2, JCZ3) allowing for user selection when running the codes [19]. With the advent of more powerful computers, selection between versions is not a necessity and the EOS is referred to as JCZ and JCZS to differentiate between the legacy code and the SNL version [20].

The JCZ3 EOS [19] is given by

$$P = \frac{G(V,T)nRT}{V} + P_0(V), \tag{2.4}$$

where P, n, R, T, and V represent the pressure, number of moles, universal gas constant, temperature, and volume, respectively. The Grüneisen function, G, and internal pressure function, P_0, are [20]

$$G = 1 - \frac{V}{f}\left(\frac{\partial f}{\partial V}\right)_T; \qquad P_0 = -\frac{dE_0}{dV}, \tag{2.5}$$

where f is a function based on Helmholtz free energy that ensures continuous behavior across a wide range of densities and E_0 is the volume potential of a face-centered cubic lattice [19]. One can see that Equation 2.4 has a form similar to an Ideal Gas with some correction factors. Hobbs et al. [12] updated the original Grüneisen function to depend on a molecular potential function, EXP6, which is similar in form to the Lennard-Jones (LJ) potential [12]. Thus, the Grüneisen function in the JCZS

EOS

$$P = \frac{G(V,T,\phi)nRT}{V} + P_0(V,\phi) \tag{2.6}$$

is based on the EXP6 function

$$\phi(r) = \epsilon \left[\left(\frac{6}{\eta - 6} \right) e^{\eta(1-r/r^*)} - \left(\frac{\eta}{\eta - 6} \right) \left(\frac{r^*}{r} \right)^6 \right]. \tag{2.7}$$

Variable η is a fit parameter which has been shown to affect the EXP6 potential relatively little [12, 20]. Due to the insensitivity of the EXP6 potential to η, most implementations use $\eta \approx 13$ [12]. The parameters r^* and ϵ are the molecular distance of separation at the minimum potential energy and well depth for the pair potential, respectively. The variable r is the distance by which the molecules are separated. The advantage of ϵ and r^* is that they can be calculated accurately from generally well characterized quantities, such as the heat of formation, molecular number, and composition. Having only two parameters to calculate makes the JCZS EOS ideal for use on a wide variety of gases [12]. The drawback of the JCZS EOS is that, while closed form, the equations require numerical differentiation and integration to compute thermodynamic states. Thus a dedicated code is required to compute the thermodynamic states desired. The JCZS EOS has been shown to provide very accurate fits to more than 750 gaseous species available through the JANNAF (Joint Army Navy NASA Air Force Interagency Propulsion Committee) tables demonstrating model efficacy across large variations in density and temperature [12]. Furthermore, a model parameter optimization study (sensitivity to η, r^*, and ϵ) across all gaseous species for densities ranging from liquids to rarified gases was performed [12, 20]. This verification work makes the JCZS equations ideal for use in constructing a set of high quality tabular thermodynamic states [12, 20].

2.1.2 SESAME Tables

The SESAME format of tabular EOS, developed by Los Alamos National Laboratory (LANL) is a flexible EOS format allowing custom table generation [23]. The TIGER code set was utilized to generate the SESAME tables for the simulations by computing equilibrium thermodynamic states over a range of temperatures and volumes representing tabular mixing for Amagat or Dalton mixtures. Construction of a mixed EOS was performed by using MATLAB scripts taking outputs of a TIGER data run from each pure gas and summing over either the volumes (Amagat) or the pressures (Dalton) from each pure gas to create a single table. Two nuances to this process are worth mentioning. Firstly, Equation 1.2 for the Amagat model is presented with volume as an extensive parameter. When summing specific volumes (an intensive parameter) sums must be weighted by mass fraction

$$v(T,P) = \sum_i w_i v_i(T,P), \tag{2.8}$$

where $w_i = \frac{m_i}{m_{tot}}$ is the i^{th} mass fraction, m_i is the i^{th} mass, and m_{tot} is the mixture total mass. Similarly, specific energy in TIGER is represented as an intensive parameter with respect to mass and is most easily summed in a mass weighted-fashion. Secondly, since specific volume is an intensive parameter, a scaling must be performed for the Dalton table. Given that the temperature and volume are the independent parameters in a Dalton mixing scheme, equivalence of state is required to get an accurate representation of the mixed pressure state. For equivalence to occur, the volumes must be equalized. Recall that

$$V = mv = Mnv, \tag{2.9}$$

where M is molecular mass. In the case of Dalton, we are considering partial pressure of each constituent at the given temperature and volume. In other words, $P_i = P(T,V)$. However, we have $P_i = P(T,v_i)$, which is equivalent, but not identical in

the sense that $V \neq v$. In order to sum over the He and SF_6 pressures for a Dalton formulation, we must demand that both pure He and SF_6 tables represent the same (T, v) states. The way to achieve this is to scale the specific volume of either the He or SF_6. Taking Equation 2.9 we can formulate a scaling factor for He volumes like so

$$m_{He}v_{He} = V = m_{SF_6}v_{SF_6} \;\Rightarrow\; v_{He} = v_{SF_6}\frac{m_{SF_6}}{m_{He}}. \tag{2.10}$$

The process used was to generate SF_6 states in TIGER and use T and scaled v values to generate the He states. The column of volume values for the He input was simply scaled as shown in Equation 2.10. A simple summation of the computed He pressures with the SF_6 pressure values at each (T, v) state was then performed.

Binary SESAME files were generated by pre-processing an input deck of the desired (T, V), or (T, P), states in MATLAB from which TIGER would calculate the temperature (T), pressure (P), specific volume (v), specific energy (e), and specific entropy (s) in that order. The resulting ASCII file was fed into the BCAT post processor within CTH, which would generate the binary file required by CTH to run the simulation with the tabular EOS. Thermodynamic states were selected based on a desire for the tables to be as general as possible without growing too large to be handled within the CTH memory constraints.

2.2 Numerical Analysis

Numerical models were developed and run in the SNL hydrocode CTH. This section discusses CTH numerical algorithms, refinement of the SESAME tables, analysis of the spatial grid, and models of the shock tube.

2.2.1 CTH

CTH was selected because it is a code that is written to study shock physics with the ability to input tabular EOS, allowing for the study of variations in customized EOS formulations [14]. The CTH solution scheme is a two step Eulerian method where the mesh first deforms with the material in a Lagrangian sense and then is mapped back to the original Eulerian positions [14]. There are six mesh options in CTH, 1D rectangular, cylindrical, and spherical coordinates, 2D rectangular and cylindrical, and 3D rectangular coordinates [14]. CTH implements the SESAME tabular EOS format in the form of binary files [14, 23].

CTH contains a set of subroutines in the BCAT module that allows for Rankine-Hugoniot analysis with a given EOS model. This permitted a study of the TIGER, Amagat, Dalton, and Ideal Gas cases. Experimental shock pressures were plotted as a function of shock speed with their corresponding error bars for direct EOS comparison [1]. The various EOS models were then interrogated to see if the shock speeds resulted in shock pressures comparable to the experimental results. This served as a check to the validity of the EOS surfaces. If a generated table could not replicate the experimental results that was indication of either an error in the table generation or inability of the EOS model to accurately resolve the shock states in the experiment. After eliminating sources of generation error, the analysis informed the user if the EOS model was useful for this problem. Furthermore, this analysis would quickly inform the user of differences and trends in the mixing models.

2.2.2 SESAME Refinement

When using a discrete representation of a continuous curve or surface the careful analyst will perform a refinement study to determine sufficient numerical resolution. Refinements to the SESAME table were handled on a basis of levels. A level describes

how small ΔT, Δv, or ΔP are. Refinement means to reduce the size of the step between temperatures, volumes, or pressures. The first level is the coarsest level with each level above it representing a halving of ΔX; X being the thermodynamic state variable of interest. For the first level, the number of thermodynamic states is computed by setting the minimum, maximum, and step size values of the state variable X using

$$N_i = \frac{X_{max} - X_{min}}{\Delta X_i} + 1, \tag{2.11}$$

where N_i is the number of values at the i^{th} level. The number of points for each variable was doubled every refinement step. Thus Equation 2.11 was rearranged to compute the step size, ΔX_{i+1} required to double the number of values

$$\Delta X_{i+1} = \frac{X_{max} - X_{min}}{2N_i - 1}. \tag{2.12}$$

Since X represents temperature and then volume, respectively, the density of points on the (T, v) surface would increase by a factor of four, for a 2D problem, with every subsequent refinement level. From ideal gas calculations the maximum shock temperature was found to be around 850 K. A SESAME table was generated with TIGER performing the mixing to estimate mixture defect from ideal behavior and help set bounds on T, v, and P. The pure He and SF_6 tables were generated for both the Amagat and Dalton mixtures. In order to provide some bound that could account for higher pressures or temperatures, $T_{max} = 1500$ K was selected. Correspondingly $T_{min} = 180$ K was chosen for the lower temperature bound. Similarly $v_{max} = 6005$ cc/g and $v_{min} = 5$ cc/g were chosen for the mixture. The initial values of ΔT and Δv were picked to provide relatively coarse spacing without being so large that many refinement levels were required for convergence. The maximum and minimum values of each property were held fixed to provide the proper refinement sequence. Table 2.1 shows the details of the first three refinements for the SESAME files. A convergence study was performed on the SESAME tables by holding the initial conditions and spatial mesh constant in 12 different shock tube configurations studied by Trueba

Table 2.1: SESAME Refinement Levels

Level	N_T	ΔT $[K]$	N_v	Δv $\left[\frac{cc}{g}\right]$
1	56	24	121	50
2	112	11.892	242	24.896
3	224	5.919	484	12.422

Monje and Yoo [1]. One of the driver pressures and one of the test section pressures pairwise in Table 2.2 defines each of the 12 cases. Shock speeds were compared via absolute relative error of the shock speeds between the different levels to assess change due to the SESAME refinement. A relative error less than 1×10^{-3} was determined to be sufficiently refined. Results showed that three refinement levels were sufficient to accurately model shock behavior. Further details are presented in Appendix B.

Table 2.2: Driver and test section pressures [1]

Driver Pressure (psia)	Test Pressure (psia)
146	1.14
166	5.70
186	11.4
-	17.1

2.2.3 Spatial Grid

Convergence with refinement of the spatial grid was also studied. The shock tube is 7.62 *cm* ID $\times$ 122 *cm* (driver) section coupled to a 7.62 *cm* square $\times$ 320 *cm* (test) section for an overall length of 442 *cm*. For level 1 the computational grid was 8 by 406 nodes, which gives a spacing of $\Delta x \approx \Delta y \approx 1.09$ *cm*. The step size refinements progressed following Equation 2.12. Table 2.3 shows the spatial refinement for the first five levels and corresponding step sizes. The results of the convergence study

are detailed in Appendix B. Methods detailed in Roache were used to estimate the convergence of the solution with mesh refinement [24]. Modeling the tube with a level 3 refinement took considerably longer to run but did not change the error much. A level 4 refinement was not run but a level 5 refinement was performed for all cases. This thesis bases its error estimates off of level 3 grids for reasons discussed below.

Simulation error to experiment was generally within single digit percentage points however a few cases were approximately 15%. A few cases were run in 3D and took quite some time to run. These cases showed significant reductions in error are realized when modeling the tube in 3D. The 3D cases were only run with a level 1 grid and showed improvement of the error from approximately 15% to less than 5%. Using a level 1 3D grid takes longer than using a refined 2D grid and was impractical for the verification and validation section of this project. The choice was made to use a 2D mesh and accept the larger error.

Table 2.3: Spatial Refinement Levels

Level	N_h	Δy $[cm]$	N_L	Δx $[cm]$
1	8	1.089	406	1.091
2	16	0.508	812	0.545
3	32	0.2458	1624	0.2723
4	64	0.1210	3248	0.1361
5	128	0.0600	6496	0.0681

2.2.4 Shock Tube Modeling

CTH models were designed to study experiments performed in the shock tube at the University of New Mexico (UNM) with a mixture of He and SF_6 [1]. The availability of this experimental data allows the numerical simulations to be validated. An input deck was written to capture the geometry of the UNM shock tube in both 1D and 2D configurations. Limited preliminary simulations were run in 3D and

the results more closely matched the experimental results. However, 3D simulations did not change the trends observed between Amagat or Dalton and would not have changed any conclusions drawn from the 2D simulations. Simulations in 3D take significantly longer to run and were unfeasible for Latin hypercube sample (LHS) analysis. Furthermore, since the trends did not change between 2D and 3D, a suite of 3D simulations was deemed unnecessary for an LHS study. A schematic image of the shock tube is provided with dimensions in Figure 2.1. Driver and test section pressures are listed in Table 2.2 and define 12 combinations pairwise. The UNM shock tube is a 7.62 *cm* ID round steel tube coupled to a 7.62 *cm* square steel tube. The round tube is the high pressure or driver section, the square tube comprises the low pressure or test section. The driver section is separated from the test section via a membrane, which is punctured by a pneumatically-driven broadhead arrow head on the axis of the driver section [1]. When the membrane is punctured the gas flow due to pressure imbalance produces a traveling planar shock wave. The test section can be easily modified to allow for pressure transducers, thermocouples, viewing windows, etc. due to its square shape (the sides are flat).

The shock wave produces a pressure and temperature spike as it passes through the test section [25]. Precise spacing of the pressure transducers allows for measurement of both the shock over-pressure and shock speed. The numerical model captures the center-line of the tube in the transverse direction in the 2D and 1D cases; thus the transition from round to square tubing is not modeled. The pressure transducers are replicated by tracers in CTH at the locations of the pressure transducers in the experiment allowing for a replication of the measurements made in the experiments. The membrane was not modeled, but assumed to vanish when it ruptured. Thus gases in the driver and test sections on either side at their respective pressures and densities were placed in contact at rupture. Just as in the experiment, in the simulation a shock was formed by the high-pressure gas moving into the low-pressure He-SF_6 mixture. The walls of the tube were implemented via a reflecting boundary

condition on 2, 4, or 6 sides depending on whether the simulation was 1D, 2D, or 3D respectively.

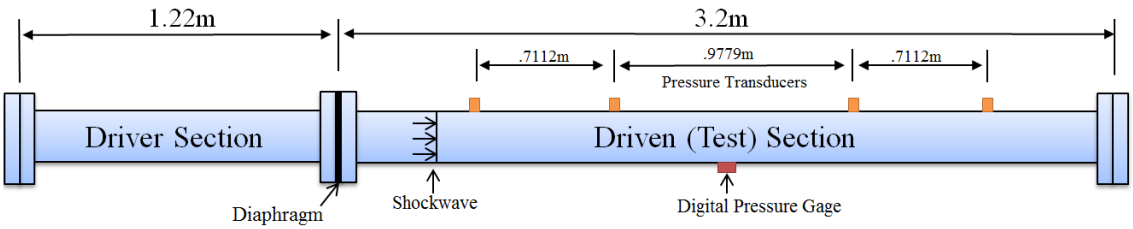

Figure 2.1: Notional depiction of UNM Shock Tube [1]

The tube was modeled with the EOS of the gas mixture as an ideal gas as well as using SESAME tables. CTH has a built-in implementation of the ideal gas relation where the user provides values for c_v and $\gamma - 1$, the specific heat at constant volume and ratio of specific heats minus one, respectively [26]. The ideal gas model was used to work out any bugs in the input decks and provide some sense of the simulation outputs. However, the question of mixing is not addressed since Dalton and Amagat are identical for ideal gases [3]. Three sets of SESAME tables were generated: one where TIGER handled the mixing of SF_6 and He, one where two pure gas tables were post processed to represent an Amagat mixture, and finally one where two pure tables were post processed to represent a Dalton mixture.

2.3 Verification and Validation

Verification of the mixture SESAME tables and spatial mesh was achieved via convergence studies. Further verification work was performed by interrogating SESAME tables and plotting surfaces to check for the correct thermodynamic surface shape.

Validation, as the name suggests, examines the accuracy of the numerical results.

For this thesis, the validation comes through comparison to the experimental results. From the experimental results, the mean values of shock speed, shock overpressure, driver pressure, and test section pressure along with their respective standard deviations are known. Thus, results based on a particular mixing law can be directly compared to the experimental results and evaluated based on the deviation from the experimental values.

From basic counting statistics of a continuous random variable we know that the standard deviation is the measure of the dispersion in a probability density function. Thus, a small standard deviation value relative to the mean indicates low dispersion in the distribution. Conversely, a large standard deviation relative to the mean indicates high dispersion in the distribution. Furthermore, the farther a simulated value is away from the experimental mean, the smaller the probability of that value occurring if the experiment were to be rerun [27, 28]. CTH predictions of the Amagat and Dalton mixtures were compared to experimental values. Experimental error bars were set at 1 standard deviation above and below the experimental measurement. This study did not perform an exhaustive analysis of the experimental methods to determine the probability of accuracy errors or systematic errors. This study seeks to investigate the difference, if any, that may occur between predictions based on two distinct mixing laws.

2.3.1 Incremental Latin Hypercubes

An incremental Latin hypercube sample (LHS) study of the inputs was performed to study variation in simulation outputs. Incremental samples mean that no input value is ever reused. This allows a convergence statement to be made about the results since values are going to begin to fill in the entire study space. The term Latin Hypercube derives from a k-dimensional extension of Latin Square sampling [29]. A Latin Square is a sparse matrix where any given row and column contains only one

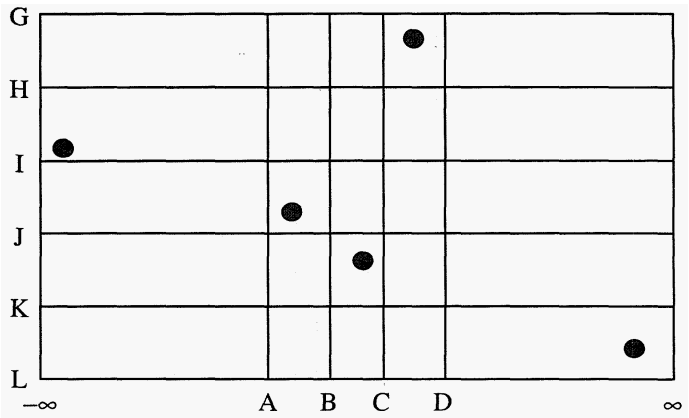

Figure 2.2: Example of a Latin Square [2]

value. An example of a Latin Square from the DAKOTA User Guide is shown in Figure 2.2, where letters A through L refer to arbitrarily selected bins of equal probability width from a probability density function [2]. Probability bins (most often in a cumulative distribution function) are successively subdivided in an incremental sampling ensuring that the tails of a distribution are accurately represented. This feature of an incremental LHS study is the second part of convergence. As more samples are run in a simulation from the LHS input 'stack', systematic variation in the inputs forces systematic variation in the output across the entire PDF. The SNL software package DAKOTA was used to generate 128,000 pseudo-random samples from distributions describing input variables used for the LHS analysis. Starting with 125 samples, simulations were run, doubling sample size every 'step'. When the correlation magnitude of input variable to shock speed, pressure, and temperature stopped changing in order and value, the simulation was determined to have converged. The driver and test sections' pressures and densities were varied along with the mass fraction of helium in the test section mixture. Parameter definitions are shown in Table 2.4 and the resulting shock pressures, temperatures, and speeds were compared for different values of variables χ_1 through χ_5 to determine sensitivity and differences the Amagat and Dalton SESAME tables. The same case was run with

both Amagat and Dalton tables so that they could be directly compared. Parameter distributions were selected based on an analysis of the experimental inputs and fitting distributions in MATLAB. If the best fit distribution was obscure or non-physical for the parameter modeled, a more physically realistic distribution was selected.

Table 2.4: Parameters to be Perturbed

Parameter	Symbol	Mean Value
Driver Pressure	χ_1	See Table 2.5
Test Pressure	χ_2	See Table 2.6
Driver Density	χ_3	See Table 2.7
Test Density	χ_4	See Table 2.8
Helium Mass Fraction	χ_5	See Table 2.9

2.3.2 Sample Selection

Distributions for each variable shown in Table 2.4 are described in this section. The decision was made to model just one of the 12 driver and test pressure combinations for the LHS study. Driver pressure 166 *psia* and test section pressure 11.4 *psia* were selected. Since the goal is to examine the sensitivity of shock tube simulations to variations in the independent variables rather than forming a comprehensive response surface, it was deemed acceptable to model only one case in the middle of driver and test section pressures.

Driver Pressure

Driver pressures from the experimental data set were analyzed with the MATLAB function *fitdist()*. The normal distribution was selected based on goodness of fit to the data (MATLAB uses the negative log-likelihood function for distribution fitting).

Mean driver pressures and standard deviations were used as inputs into DAKOTA to define the parameter distributions. Table 2.5 details three different nominal driver pressures and the corresponding normal distribution parameters. The decision was made to bound the normal distributions at $\pm 3.08\sigma$ for each case, including $\pm 3.08\sigma$ corresponds to 99.8% of expected values [27]. The formula for the normal distribution is

$$f(x) = \frac{1}{\sigma\sqrt{2\pi}} \exp\left[-\frac{(x-\mu)^2}{2\sigma^2}\right], \tag{2.13}$$

where μ is the mean and σ is the standard deviation.

Table 2.5: χ_1 (Driver Pressure) Normal Distribution Fits

Case	μ $\left[\frac{dyne}{cm^2}\right]$	σ $\left[\frac{dyne}{cm^2}\right]$	- Bound $\left[\frac{dyne}{cm^2}\right]$	+ Bound $\left[\frac{dyne}{cm^2}\right]$
146 psia	10.06977×10^6	5.537×10^3	10.05272×10^6	10.08682×10^6
166 psia	11.44710×10^6	13.283×10^3	11.40619×10^6	11.48801×10^6
186 psia	12.82305×10^6	6.013×10^3	12.80453×10^6	12.84158×10^6

Test Section Pressure

Because experimental test section pressures varied little, $\sigma \approx \mathcal{O}(10^{-16})$, a triangular distribution

$$f(x) = \begin{cases} 0 & b < x \text{ or } x < a \\ \frac{2(x-a)}{(b-a)(c-a)} & a \leq x < c \\ \frac{2}{b-a} & x = c \\ \frac{2(b-x)}{(b-a)(b-c)} & c < x \leq b \end{cases} \tag{2.14}$$

was used. The triangular distribution is defined with minimum and maximum values, a and b, respectively, and mode, c ($a \leq c \leq b$). Test pressure distribution parameters are shown in Table 2.6. The upper and lower bounds, b and a, respectively,

correspond to a variation of ± 0.2 *psia*[1], about the same as the worst case variation seen in the driver section.

Table 2.6: χ_2 (Test Pressure) Triangular Distribution Fits

Case	a $\left[\frac{dyne}{cm^2}\right]$	b $\left[\frac{dyne}{cm^2}\right]$	c $\left[\frac{dyne}{cm^2}\right]$
1.14 psia	6.4811×10^4	9.2390×10^4	7.8600×10^4
5.70 psia	37.9212×10^4	40.6791×10^4	39.3001×10^4
11.4 psia	77.2213×10^4	79.9792×10^4	78.6002×10^4
17.1 psia	116.5214×10^4	119.2793×10^4	117.9003×10^4

Driver and Test Section Densities

CTH requires the independent thermodynamic values of an input deck for our problem to be pressure and density. In the experiment, pressure and temperature were measured directly. Thus the SESAME tables were interrogated to determine the range of the densities based on the range in the temperature ($T \in [293.305, 297.155]$ K) at the pressures listed in Table 2.2 for the test section. The driver densities shown in Table 2.7 are fitted with a triangular distribution as described in Equation 2.14. Pure helium gas was used for the experiments as the driver section gas. Since pure helium behaves as an ideal gas over the range of pressures and temperatures simulated the densities could be computed directly from Equation 2.1. Test section densities were also modeled with the triangular distribution and the distribution parameters are shown in Table 2.8.

Helium Mass Fraction

Helium mass fraction was varied to simulate uncertainty in the experimental mixing. Bounded normal distribution parameters used to simulate this variance are shown

[1]A pressure of 1 *psia* $\approx 68,947.55$ $\frac{dyne}{cm^2}$

Table 2.7: χ_3 (Drive Densities) Triangular Distribution Fits

Case	a $\left[\frac{g}{cm^3}\right]$	b $\left[\frac{g}{cm^3}\right]$	c $\left[\frac{g}{cm^3}\right]$
146 psia	1.6304×10^{-3}	1.6518×10^{-3}	1.6410×10^{-3}
166 psia	1.8537×10^{-3}	1.8780×10^{-3}	1.8658×10^{-3}
186 psia	2.0770×10^{-3}	2.1043×10^{-3}	2.0906×10^{-3}

Table 2.8: χ_4 (Test Density) Triangular Distribution Fits

Case	a $\left[\frac{g}{cm^3}\right]$	b $\left[\frac{g}{cm^3}\right]$	c $\left[\frac{g}{cm^3}\right]$
1.14 psia	3.2887×10^{-4}	3.3468×10^{-4}	3.3176×10^{-4}
5.70 psia	11.6073×10^{-4}	14.8748×10^{-4}	13.2230×10^{-4}
11.4 psia	23.1943×10^{-4}	27.9275×10^{-4}	25.5376×10^{-4}
17.1 psia	34.7671×10^{-4}	39.9328×10^{-4}	37.3208×10^{-4}

in Table 2.9.

Table 2.9: χ_5 (Helium Mass Fraction) Normal Distribution Fits

μ	σ	- Bound	+ Bound
0.0267	0.0033	0.0165	0.0369

The upper and lower bounds were selected based on estimates of variation in the He mole fraction

$$x_{\mathrm{He}} = \frac{n_{\mathrm{He}}}{n_{\mathrm{He}} + n_{\mathrm{SF_6}}}, \tag{2.15}$$

where n_i is the number of moles of component i. Utilizing the relation $m = nM$ allows Equation 2.15 to be transformed into a form dependent on mass fraction w_{He}.

$$x_{\mathrm{He}} = \frac{1}{1 + \frac{M_{\mathrm{He}}}{M_{\mathrm{SF_6}}}\left(w_{\mathrm{He}}^{-1} + 1\right)}. \tag{2.16}$$

For $w_{\mathrm{He}} = 0.0267 \pm 0.01$ the mole fraction takes on the values $x_{\mathrm{He}} \approx [0.38, 0.58]$, which could have a significant affect on the shock characteristics.

Chapter 3

Results

All 12 experimental nominal pressure combinations were simulated in CTH. During the course of the analysis it became convenient to express the shock speed and shock temperature as functions of the dimensionless pressure ratio

$$\phi = \frac{P_{\text{Driver}}}{P_{\text{Test}}}. \tag{3.1}$$

Nominal pressures are used to determine the value of ϕ, which had the convenient effect of allowing shock speed and shock temperature results to each be displayed on single curves. Plotting the shock speeds and shock temperatures a function of ϕ allowed graphical analysis of the differences between the Amagat and Dalton formulations. Pressure ratios used are listed in Table 3.1.

Shock speed, temperature, and pressure are not simple functions of pressure ratio. Rather, the thermodynamic characteristics of what is driving the shock as well as the gas mixture into which the shock is traveling determine measured shock speeds, pressures, and temperatures. This became clearly evident after it was discovered that the experimental work had used pure helium as driver gas while preliminary numerical simulations assumed a driver gas of 50:50 molar mixture of helium and SF_6, resulting in wildly different shock characteristics. Furthermore, shock pressure

Table 3.1: Pressure Ratios

ϕ	P_{Driver} $[psia]$	P_{Test} $[psia]$
128.1	146	1.14
25.6	146	5.70
12.8	146	11.4
8.5	146	17.1
145.6	166	1.14
29.1	166	5.70
14.6	166	11.4
9.7	166	17.1
163.2	186	1.14
32.6	186	5.70
16.3	186	11.4
10.9	186	17.1

is not well described as a function of a pressure ratio, but rather as a surface that is described by both driver and test section pressures.

3.1 EOS Verification

EOS surfaces were analyzed prior to running simulations in CTH to ensure that they passed through the thermodynamic states of interest. The BCAT subroutine allows for Rankine-Hugoniot analysis of an EOS, which permitted a direct comparison of shock speed and shock pressure from the experiment. Rankine-Hugoniot results are shown in Figure 3.1.

In general, Amagat formulation data (diamond points) most closely matches experimental values, which are shown with error bars. SESAME tables computed directly from TIGER mixing and Dalton mixing most closely match one another (circle and square points, respectively). All data points are relatively close to the experimental values demonstrating the ability of every SESAME EOS used to approximately pass through the shock states measured in the experiment. TIGER EOS files were only

used for mesh refinement and getting a sense of non-ideal behaviors in the mixture. This work was completed while mixing scripts were in development for the Amagat and Dalton SESAME tables.

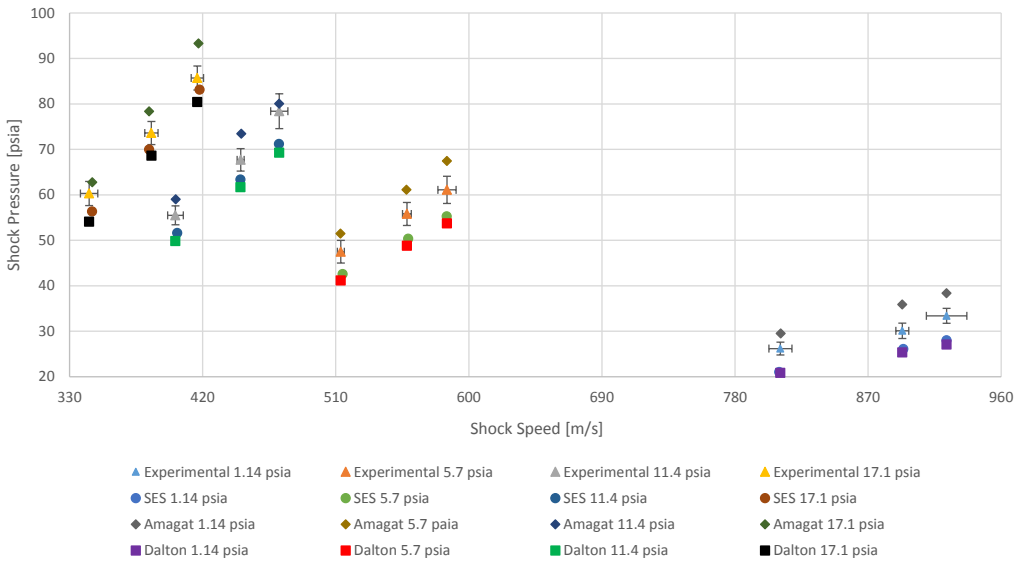

Figure 3.1: Comparison of EOS Shock States via Rankine-Hugoniot Analysis

3.2 Spatial Grid

Simulation grids were refined to study the amount of error associated with the spatial mesh. During the course of the study it was determined that Richardson extrapolation would not work since CTH changes the first and second coefficients of viscosity to enforce numerical stability across the shock front. This prompted a level 5 mesh to be run for all 12 experimental cases to look for changes in the shock speed, pressure, and temperature as a function of a highly refined grid. The results of the level 5 simulations showed that Level 5 simulation results were very close in value to the level 1, 2, and 3 results.

Simulated shock speeds were not monotonic with mesh size, indicating that it is most affected by changes to viscosity coefficients and so, extrapolations were not very helpful. Instead the value of the shock speed was compared between the mesh levels 2 and 3 described in Table 2.3. Numerical error is presented in Table 3.2 and is the absolute percent error relative to f_3.

Table 3.2: Shock Speed Refinement Error

ϕ	f_2 $[m/s]$	f_3 $[m/s]$	$\lvert\varepsilon_{23}\rvert$
128.1	932.8933	932.2836	0.065%
25.6	602.2975	601.7222	0.096%
12.8	483.6105	483.3302	0.058%
8.5	422.0700	421.8304	0.057%
145.6	961.9362	961.6693	0.028%
29.1	626.1377	625.7848	0.056%
14.6	504.2622	504.0943	0.033%
9.7	441.0974	440.8154	0.064%
163.2	988.2076	987.5557	0.066%
32.6	647.7944	647.2558	0.083%
16.3	523.2217	523.0088	0.041%
10.9	458.4630	458.1232	0.074%

Shock pressure and temperature behaved more like one would expect with spatial grid refinement. The simulated values were generally monotonic with mesh refinement and showed something like $\mathcal{O}(h)$ convergence with some notable exceptions. However, due to the nature of the changing coefficients of viscosity extrapolation values do not tell the whole story. Tables 3.3 and 3.4 show the absolute percent error relative to levels 2 and 3. There is very little difference between the levels indicating that additional spatial refinement is not needed. A level 5 mesh produced shock pressures and temperatures very similar to the level 1, 2, and 3 mesh results.

Table 3.3: Shock Pressure Refinement Error

ϕ	f_2 $[psia]$	f_3 $[psia]$	$\lvert\varepsilon_{23}\rvert$
128.1	28.6965	28.6911	0.019%
25.6	58.6622	58.6610	0.002%
12.8	74.6633	74.7866	0.165%
8.5	83.7313	83.8758	0.172%
145.6	30.5326	30.5253	0.024%
29.1	63.4755	63.4749	0.001%
14.6	81.6538	81.6727	0.023%
9.7	91.8446	91.9482	0.113%
163.2	32.2185	32.2115	0.022%
32.6	67.9922	67.9923	0.000%
16.3	88.0465	88.0270	0.022%
10.9	99.6717	99.8062	0.135%

Table 3.4: Shock Temperature Refinement Error

ϕ	f_2 $[K]$	f_3 $[K]$	$\lvert\varepsilon_{23}\rvert$
128.1	717.703	716.580	0.157%
25.6	486.813	484.837	0.408%
12.8	420.023	419.908	0.027%
8.5	388.784	388.821	0.010%
145.6	741.819	740.513	0.176%
29.1	500.991	498.917	0.416%
14.6	431.265	430.613	0.151%
9.7	397.877	397.828	0.012%
163.2	763.953	762.390	0.205%
32.6	514.209	512.411	0.351%
16.3	441.636	440.482	0.262%
10.9	406.540	406.503	0.009%

3.3 Shock Tube Simulations

Shock tube simulation outputs were analyzed via MATLAB scripts to determine shock quantities of interest (QoI), namely shock speed, pressure, and temperature.

Analysis was performed via MATLAB scripts which looked for change in velocity at the tracer for shock speed and maximum temporal derivatives for post-shock temperature and pressure. More information on MATLAB scripts is presented in Appendix C.

3.3.1 Shock Speed, U_s

We found by inspection of the plots and by curves of best fit, that Amagat and Dalton results converge as the pressure ratio approaches unity. This makes some intuitive sense as there is not as much disparity in pressure energy between the drive and test gases. Thus, there is less ability of the drive section to push on the test section, resulting in weaker shocks that propagate more slowly. In addition, both the drive and test sections were initialized in the simulation at room temperature ($295\ K$). Thus any increase in energy must come solely from the pressure imbalance. This is most evident in the trends shown by shock speed as a function of pressure ratio shown in Figure 3.2. As is shown, the higher the pressure ratio, the faster the shock speed. Both Amagat and Dalton simulation data was fit using a curve of best fit of the form $U_s(\phi) = a\ln(\phi) + b$. Best fit coefficients were determined using linear least squares and the value of the coefficient of determination was computed, resulting in a value of approximately 0.95. Grouping in clusters of three is due to distinct groupings of the pressure ratios as is shown in Table 3.1. One will notice that the data points do not fall exactly onto the logarithmic curves. This is due to the fact that some information about the shock speed is contained in the test section pressure and density. To fully describe the shock speed, one needs more than one dimension.

The curves nicely capture the Amagat and Dalton trends and show that Dalton tends to overestimate the experiment when using the same pressures and initial temperatures. For the purposes of investigating the differences between the mixing

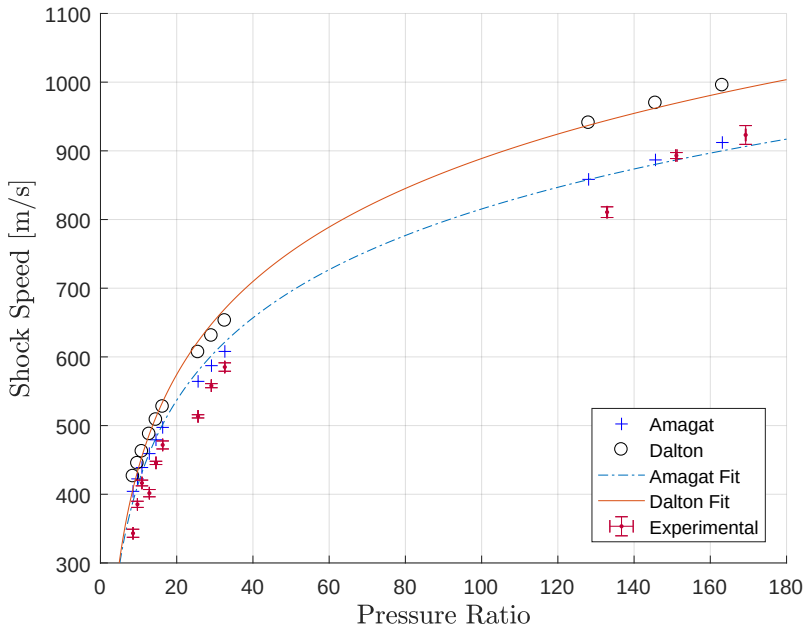

Figure 3.2: Shock Speed Versus Pressure Ratio

models, we find that using pressure ratio is a good way to compare the results. However, we do not claim that a fit based on pressure ratio alone is necessarily a good predictor of shock tube results. As one achieves higher pressure ratios in the shock tube, the disparity between Amagat and Dalton models becomes more pronounced indicating that Amagat and Dalton predictions may diverge further with even higher pressure ratios. Error between simulation and experimental results is shown in Table 3.5. Error was calculated using a normalized difference

$$\varepsilon = \frac{x_{experimental} - x_{simulated}}{x_{experimental}} \cdot 100\%, \tag{3.2}$$

where $x_{experimental}$ is the measured value and $x_{simulated}$ is the simulated value. As is shown in Figure 3.2 and Table 3.5, the 2D simulation tends to have lower error at higher pressure ratios. At some of the lower pressure ratios the error is unacceptably high, however, this may be overcome by running the simulations in 3D instead of 2D. Overall, Amagat simulation values match experiment better than Dalton simulation values. Error is primarily reduced by modeling the transition from round to square

tubes for the driver and test sections, which requires a 3D simulation. 3D simulations were run to verify error reduction and look at trends in the shock states. The error for pressure ratios 8.5, 9.7, and 12.8 is the highest. These pressure ratios along with $\phi = 128.1$ were run in 3D to assess results. Due to eddies produced by the transition from round to square tubing, the shock QoI had to be extracted by hand from the data due to ringing in the pressure and temperature values. Furthermore, running 3D causes mesh size to grow by a factor of 8 with every refinement level making refinement take significantly longer. The four cases run reduced the error to less than 5% using a level 1 mesh and matched the observed trends from the 2D simulations.

Table 3.5: Simulation Shock Speed Error

ϕ	Amagat	Dalton
128.1	-5.89%	-13.83%
25.6	-9.91%	-15.41%
12.8	-14.34%	-17.65%
8.5	-17.78%	-19.50%
145.6	0.71%	-7.89%
29.1	-5.22%	-11.55%
14.6	-7.54%	-12.37%
9.7	-9.62%	-13.43%
163.2	1.19%	-7.27%
32.6	-3.88%	-10.37%
16.3	-5.41%	-10.58%
10.9	-5.41%	-9.96%

3.3.2 Shock Pressure, P_s

Shock pressures shown in Figure 3.3 are separated by test section pressure. Plotting shock pressures versus pressure ratio ϕ does not result in a curve similar to those for shock speed shown in Figure 3.2. One can see that, unlike the shock speeds, shock pressures are underestimated by the Dalton method. However, trends hold in

that the Dalton and Amagat results do not cross and the disparity in the predictions grows with increasing pressure ratio. Indicating the Amagat and Dalton EOS surfaces predict different thermodynamic states across the range of pressure ratios with increasing disparity at more extreme pressure ratios.

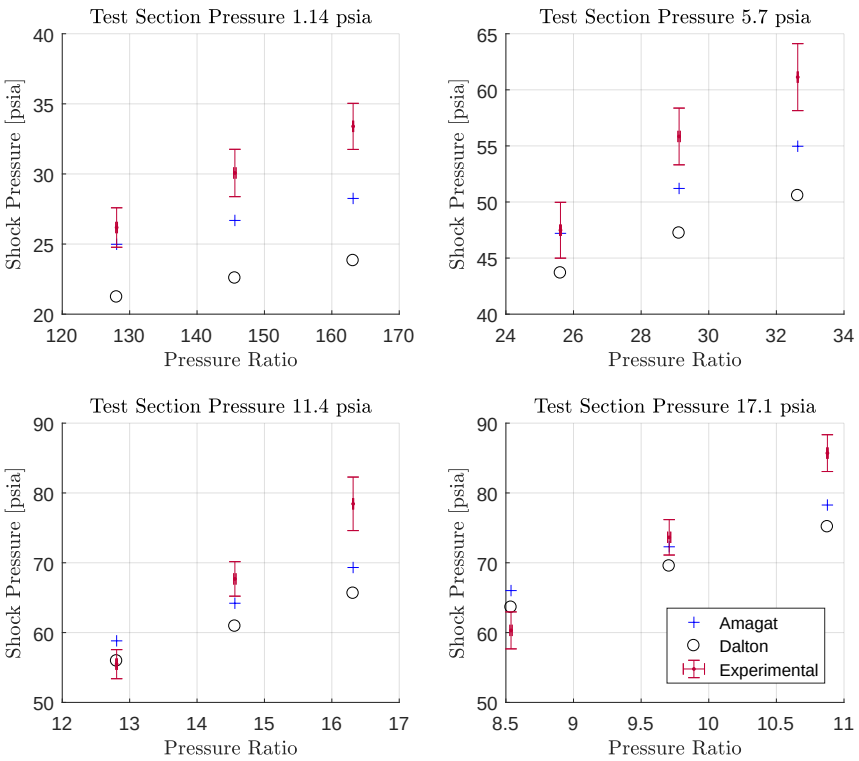

Figure 3.3: Shock Pressure Into Various Test Section Pressures

Experimental values cross over the two models at low values of ϕ. This may be because of error inherent in the 2D simulation or model form error inherent to Amagat and Dalton mixtures. In general, Amagat tends to be the better predictor of shock pressure. However, one may note that the difference between Amagat and Dalton predictions is nearly constant with pressure ratio for each test section pressure. Simulation error with respect to experiment is tabulated in Table 3.6 shows that the Amagat method is the better predictor of shock pressure with the notable exceptions of $\phi = 8.5$ and $\phi = 12.8$. Unlike the shock speed, error improves with lower

pressure ratios. Most of the errors are $< 10\%$ indicating that Amagat is relatively accurate. However, at certain values of ϕ the error is as high as 15%. Running more computationally expensive 3D models would reduce this error as discussed previously if very accurate models of the shock tube were desired.

Table 3.6: Simulation Shock Pressure Error

ϕ	Amagat	Dalton
128.1	4.57%	23.34%
25.6	0.58%	8.72%
12.8	-6.02%	-0.83%
8.5	-9.45%	-5.21%
145.6	11.26%	33.20%
29.1	8.30%	18.24%
14.6	5.15%	11.11%
9.7	1.84%	5.91%
163.2	15.39%	40.19%
32.6	10.08%	20.89%
16.3	11.63%	19.52%
10.9	8.67%	14.03%

3.3.3 Shock Temperature, T_s

Shock temperatures were not measured in the initial experimental work. Simulated temperatures are shown in Figure 3.4 plotted versus pressure ratio. The dependence on the test section pressures becomes apparent in Figure 3.4 as the groups of data points have a more pronounced defect from the curves of fit. As with shock speed, shock temperatures were fit with curves of the form $T_s(\phi) = a\ln(\phi)+b$. Calculation of the coefficient of determination resulted in a value of approximately 0.91. The trend continues to hold that Dalton and Amagat are clearly different without crossing each other over the range of pressure ratios studied.

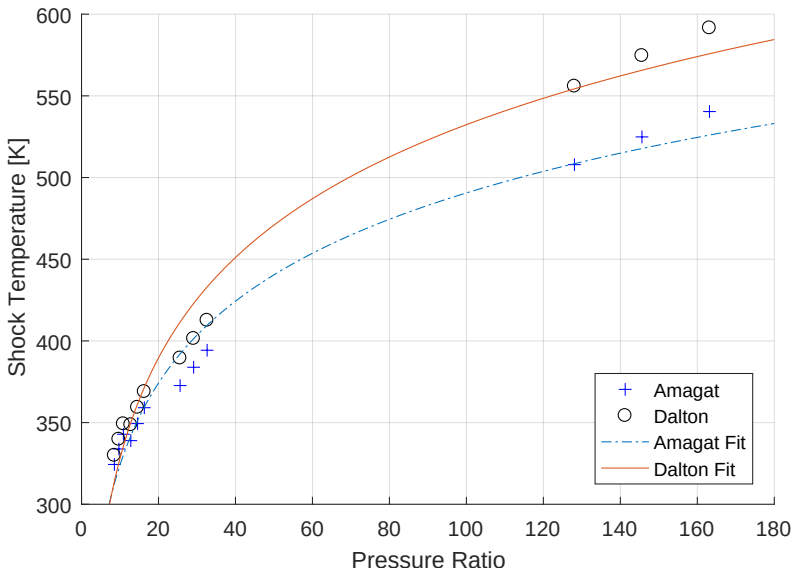

Figure 3.4: Shock Temperature Versus Pressure Ratio

3.4 LHS Analysis

LHS results for $\phi = 14.6$ were analyzed using the MATLAB function *corrcoef()* in an incremental fashion. The base sample set consisted of 125 pseudorandom samples and the number of samples doubled with every 'step'. Starting with the base sample set of 125 values the magnitude of the correlation coefficient, r, was computed using *corrcoef()*, against U_s, P_s, and T_s and χ_1 through χ_5 in a pairwise manner for every doubling.

Once the order and the magnitude of the correlation for the statistically significant variables stopped changing, the study was deemed to have converged. Histograms of the correlation of the shock speeds, U_s, pressures, P_s, and temperatures, T_s, to independent variables χ_1 through χ_5 were plotted to determine convergence. Simulation results converged after 1000 samples (three doublets) of each variable were run as defined in Table 3.7.

Table 3.7: Parameters Perturbed in LHS Study

Parameter	Symbol	Mean Value
Driver Pressure	χ_1	11.44710×10^{6} $dyne/cm^2$
Test Pressure	χ_2	78.6002×10^{4} $dyne/cm^2$
Driver Density	χ_3	1.8658×10^{-3} g/cm^3
Test Density	χ_4	25.5376×10^{-4} g/cm^3
Helium Mass Fraction	χ_5	0.0267

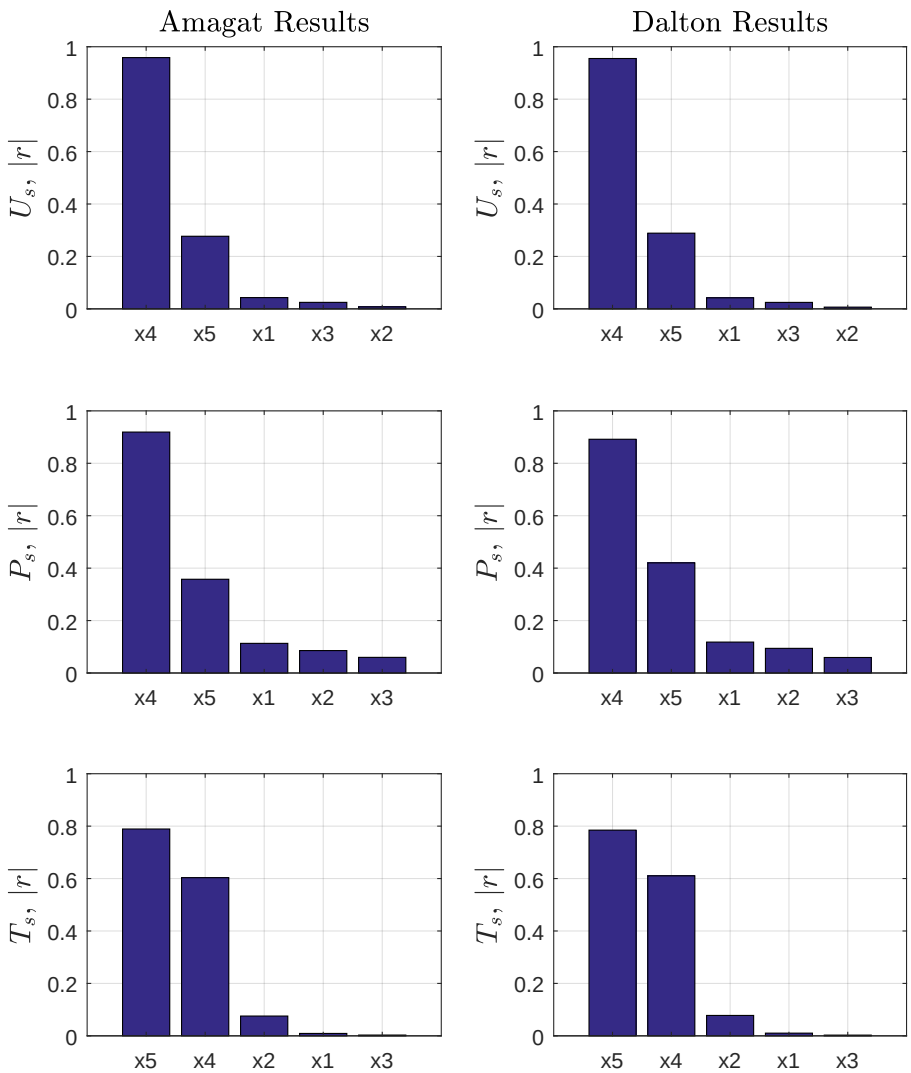

Figure 3.5: LHS QoI Results Run Against 1000 Samples

Figure 3.5 shows the final results of the LHS study summarized with Amagat and Dalton QoI (Quantities of Interest) in the left and right columns, respectively. As is shown both the Amagat and Dalton models are most sensitive to χ_4, test section density, and χ_5, helium mass fraction. However, which variable has the strongest relationship depends on the QoI. The sensitivity of the two models is quite similar in magnitude and ordering of variables, χ_i, based on the correlation strength. Only shock pressure shows a significant difference in sensitivity between the Amagat and Dalton models in the second-most influential paramters χ_5, helium mass fraction.

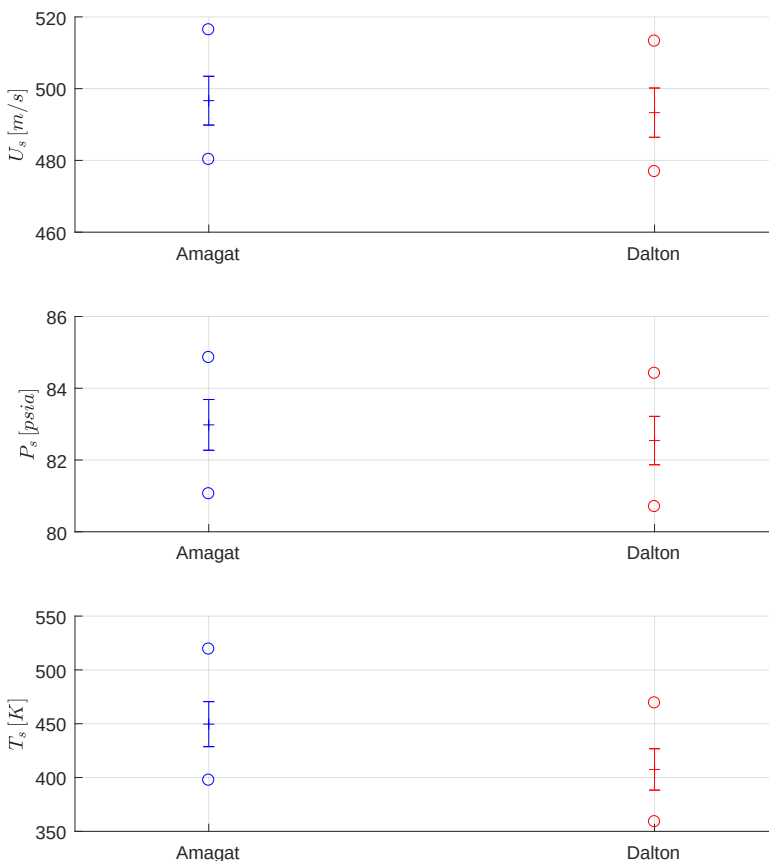

Figure 3.6: Comparison of Amagat and Dalton LHS Results

Statistics of the LHS results of Amagat and Dalton mixtures are shown in Figure 3.6. The minimum, mean, and maximum values are superimposed on a plot of standard

deviation ($\pm 1\sigma$) of each mixing model for each QoI. Unlike the results in Section 3.3 compared to experimental values, the Amagat model predicts faster shock speeds, higher shock pressures, and higher shock temperatures overall than the Dalton model does for the same initial pressures and densities. Simulations for the LHS study were run for the same initial pressures and densities which resulted in different initial temperatures of the test section mixture for the Amagat and Dalton models. Recall that CTH requires the initial pressure and density or temperature and density to be specified. In simulations compared to experimental results in Section 3.3, density was set from experimental initial pressure and temperature. This led to different initial density values depending on whether an Amagat or Dalton EOS was used. Differences between shock speed and pressure distributions are not large, with shifts of 5 m/s and 1 $psia$, respectively. However, a difference of roughly 50 K is seen in the shock temperature predictions, which is significant for the given shock regime.

Results from CTH simulations show that for the same input values, Amagat and Dalton EOS mixtures will predict different shock characteristics. Another way to think about the problem is to ask, 'if simulation initial conditions were perturbed in the Amagat and Dalton simulations, how much would the models agree?' This is shown to some degree in Figure 3.6, but does not yield a quantitative result. Using the MATLAB function *fitdist()*, we fit the LHS study QoI with probability density functions (generalized extreme value) over their respective range of values. We then calculated the coefficient of overlap, C_{ovl}, between the two distributions and plotted the results [30, 31].

3.4.1 Shock Speed, U_s

Figure 3.7 shows that there exists strong agreement between the Amagat and Dalton EOS when it comes to predicting the shock speed. The overlap between the two distributions comprises 80.58% of the simulated values based on the value of C_{ovl}.

One way of thinking about this result is that that the distance between the Amagat and Dalton shock speed distributions is not large.

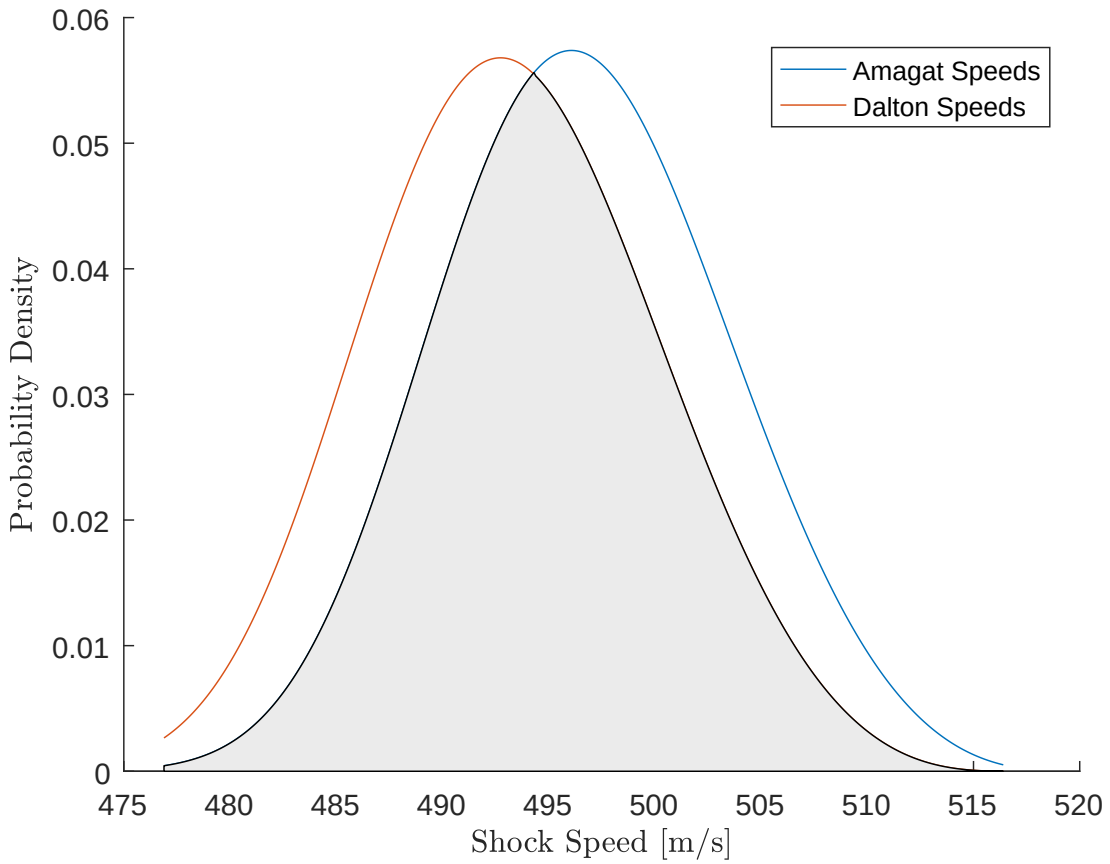

Figure 3.7: Overlap in Shock Speed Distributions, $C_{ovl} = 0.8058$

3.4.2 Shock Pressure, P_s

Similarly, shock pressures were analyzed are shown in Figure 3.8. The results show that the pressures also have strong agreement, as the overlap constitutes 75.27% of the simulated values. While slightly less than shock speed overlap, the agreement between the two distributions is still significant.

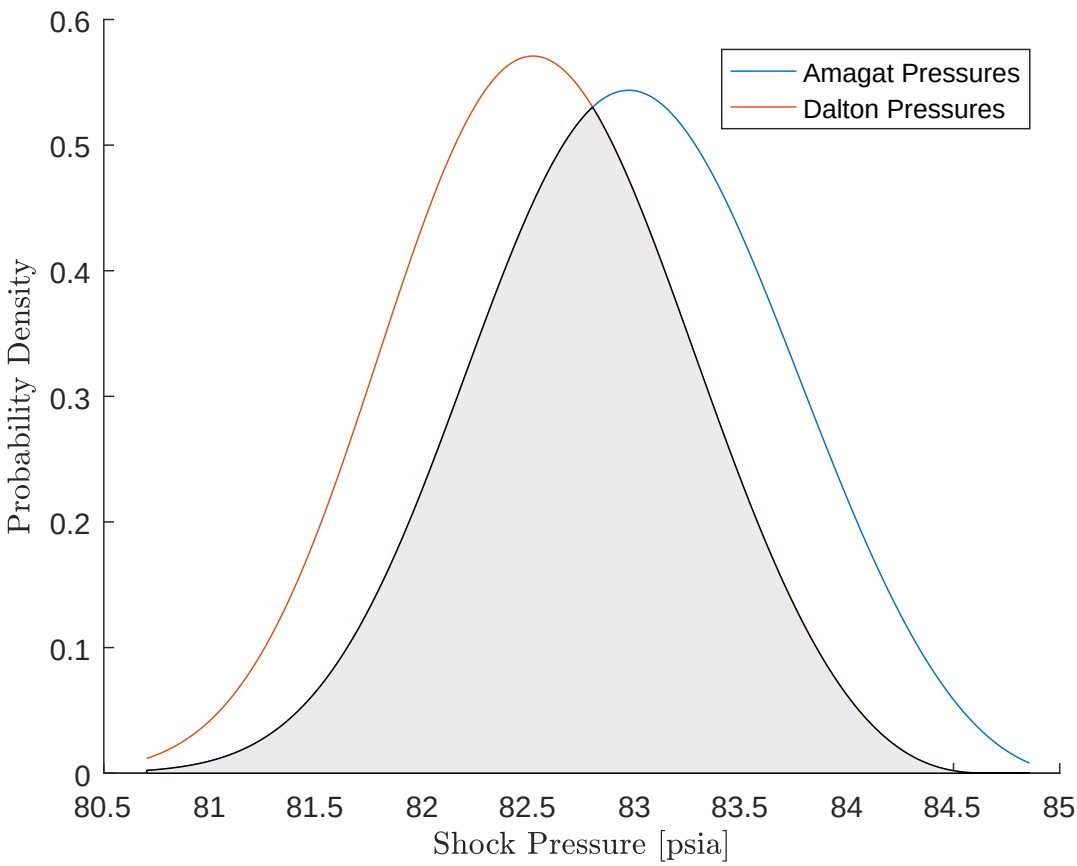

Figure 3.8: Overlap in Shock Pressure Distributions, $C_{ovl} = 0.7527$

3.4.3 Shock Temperature, T_s

The shock temperatures showed the most disparity between the two models as the overlap only accounted for 29.02% of the simulated values. Figure 3.9 shows the two temperature distributions and the region of overlap. This is the strongest difference between the two models.

In summary, we have shown that the Amagat mixing model provides the best agreement with the experimental results and that those results are distinctly different

from the Dalton model. Furthermore, we have shown that for the same initial conditions the Dalton model will tend to overpredict the experimental values as opposed to LHS values where it underestimates shock QoI. We believe that the reason for Dalton overestimation had to do with the way CTH requires initial conditions be set as pressure and density versus pressure and temperature. Thus, when the shocktube was simulated, different densities would be provided depending on the EOS so that the simulations started off at the same temperature. Finally, when comparing perturbations of the initial conditions we show that the strongest disparity between the simulated results occurs in the prediction of shock temperature.

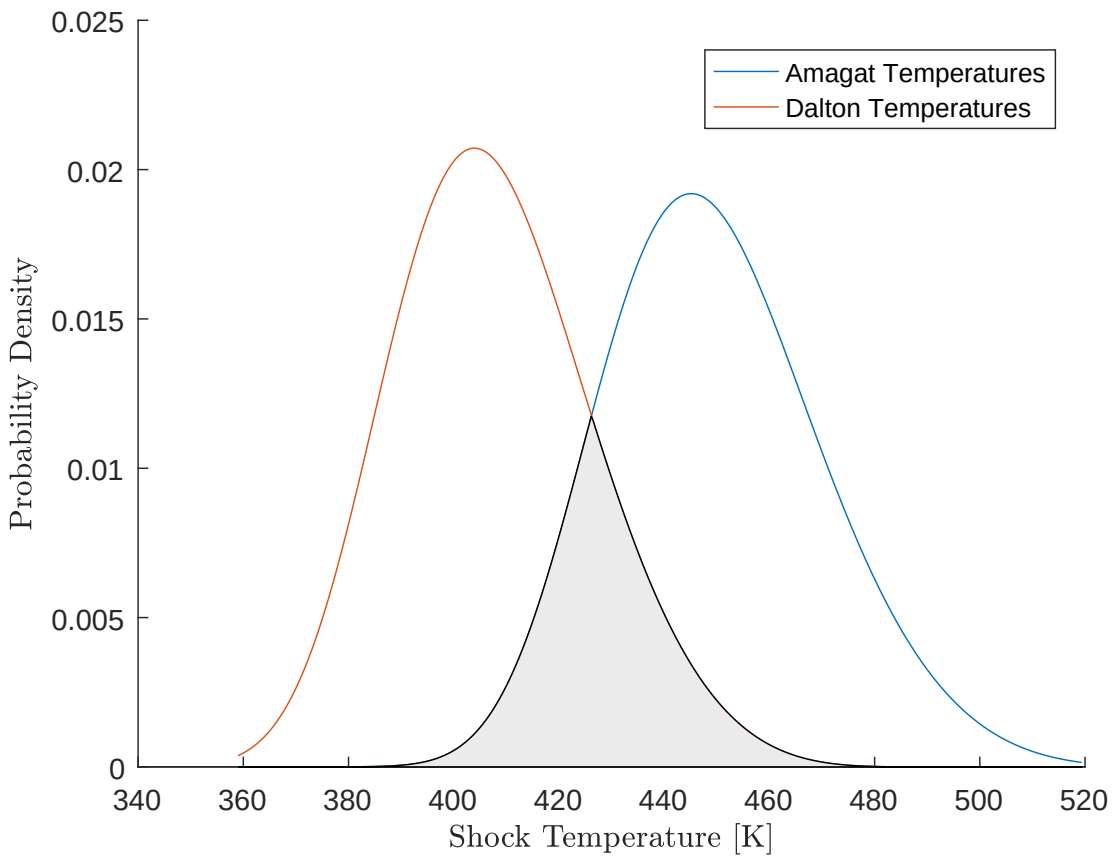

Figure 3.9: Overlap in Shock Temperature Distributions, $C_{ovl} = 0.2902$

Chapter 4

Conclusions & Future Work

4.1 Conclusions

Based on the modeling of the shock tube as shown in Figures 3.2, 3.3, and 3.4 we conclude that there is a difference between the Amagat and Dalton EOS models. The greatest differences occur when looking at the shock speed and shock temperature. This can be explained, as was noted in Chapter 3, by the fact that the densities were used to set the temperature of the simulation. By setting the same pressures and different densities to achieve the same temperatures, we were acknowledging that the EOS surfaces were predicting different thermodynamic states for the mixture. This affected the outcomes as has been shown. LHS results show the strongest agreement between Amagat and Dalton models in the shock speed and the worst agreement in the shock temperatures. In addition, the LHS results showed that the shock pressure has the most complicated relationship to the input parameters perturbed. Shock speed and shock temperature were dominated by variables χ_4 and χ_5. Shock pressure, while still predominately dependent on χ_4 and χ_5, has a stronger relationship with χ_1, χ_2, and χ_3 than either shock speed or shock temperature. This can be seen in

the magnitudes of the correlation coefficients in Figure 3.5. Furthermore the LHS analysis showed that while the Amagat and Dalton EOS models were sensitive to essentially the same parameters, it also showed that both predict different shock speeds, pressures, and temperatures. The only way to get agreement between the shock characteristics is to allow the initial conditions to vary. Experience running the simulations has shown that the forcing agreement may require nonsensical initial conditions in the simulation, which defeats the purpose of modeling. As was shown in Figures 3.7, 3.8, and 3.9 the models only agree well on 2 out of the 3 characteristics. This implies that the models cannot simultaneously agree on both pressure and temperature of the mixture. If agreement is forced in the temperatures, the pressure will fail to agree and vice versa. When modeling inert gases undergoing shocks, we see that Amagat and Dalton mixing do not give the same results. In general the Amagat model results are in significantly better agreement with the experimental data for shock speed and shock pressure. Forthcoming experimental results for shock temperature will be important in assessing whether one model is clearly superior in predicting results for mixed gases undergoing shock.

4.2 Future Work

In the course of performing research one finds out how very little they are able to push the boundary of knowledge, even when expending considerable amounts of effort and resources. There is usually more work to do and, in the very least, refinements to be made. This work could be improved and expanded in a number of ways:

- Run more LHS studies to develop mixing response surfaces
- Study other gaseous mixtures
- Study reacting gases or ionizing gases (TIGER can model ionized gases)

- Look at mixtures with more than two constituents
- Consider some form of phase change

One advantage of LHS studies, is that they provide insight into which parameters drive variation in the model. One way in which this work could be used would be to explore how restricting the variation of the LHS input distributions affect results.

The preceding list only begins to scratch the surface possible improvements or additions. This research showed that a difference exists between Amagat and Dalton mixtures but further development is needed to understand how the differences affect predictions. In addition, the LHS analysis showed that test section density and mixture mass fraction had strong influence over the shock speed, pressure, and temperature. This could inform new experiments by better controlling either variable and then adding in known variations. One example would be heating or cooling the test section to achieve different shock speeds. Addressing model form error by parametrizing χ_4 and χ_5 would mitigate, or at least provide control over, model sensitivity in the Amagat and Dalton representations. This could take many forms and may be an avenue for research that would provide insight into mixture physics. Finally, extending this work to other gases may help formalize good modeling and simulation practices in the realm of gas dynamics.

Appendices

Appendix A

Sample CTH Input

Below is a sample of a CTH input deck used in the simulations performed in this research.

```
*************************************************************************
*eor* cthin
*
*************************************************************************
Shocktube with He and SF6 Dalton SESAME EOS Refinement Level 3
* Mesh Level 1
* Driver pressure: 1.1458e+07
* Driver density: 1.8596e-03
* Test pressure: 7.9047e+05
* Test density: 2.4731e-03
control
    mmp
    tstop = 8.5e-3
endc
```

```
spy

PlotTime(0.0, 50e-5);

SaveTime(0.0, 10e-5); Save("M,VOLM,VX,VY,P,T");

ImageFormat(1024,768);

define main()
{
pprintf(" PLOT: Cycle=%d, Time=%e\n",CYCLE,TIME);
XLimits(0,442);
YLimits(0,7.62);
Image("Pressure");
Window(0,0,0.75,1);
ColorMapRange(1e4,2e7,LOG_MAP);
Label(sprintf("Pressure at %0.2e s.",TIME));
Plot2D("P");
Draw2DMatContour;
Draw2DTracers(3);
DrawColorMap("(dyn/cm2̂)̂",0.75,0.4,0.9,0.9);
EndImage;

Image("Vmag");
Window(0,0,0.75,1);
ColorMapRange(1e1,1e10,LOG_MAP);
Label(sprintf("Velocity Magnitude at %0.2e s.",TIME));
Plot2D("VMAG");
Draw2DMatContour;
Draw2DTracers(3);
DrawColorMap("(cm/s)",0.75,0.4,0.9,0.9);
```

```
EndImage;

Image("Temperature");
Window(0,0,0.75,1);
ColorMapRange(0,.07);
Label(sprintf("Temperature at %0.2e s.",TIME));
Plot2D("T");
Draw2DMatContour;
Draw2DTracers(3);
DrawColorMap("(eV)",0.75,0.4,0.9,0.9);
EndImage;
}

HisTime(0,1e-6);
SaveTracer(ALL);
SaveHis("GLOBAL,POSITION,P,T,DENS,VX,VY");

define spyhis_main()
{
HisLoad(1,"hscth");
Label("Pressure at Tracer 1");
TPlot("P.1",1,AUTOSCALE);
Label("Pressure at Tracers 2-6");
TPlot("P.2",1,AUTOSCALE);
TDraw("P.3",1);
TDraw("P.4",1);
TDraw("P.5",1);
TDraw("P.6",1);
}
endspy
```

```
mesh
*
block 1 geom=2dr type=e
*
  x0 0.
    x1 n=408 ratio=1 w=442
  endx
*
  y0 0.
    y2 n=8 ratio=1 w=7.62
  endy
endb
*
endm

convct
    interface=smyra
endc
*********************************************************************
*
* equation of state inputs
*
eos SES=500000
      mat1 SES USER EOS=9997 FEOS='b9997'
      mat2 IDGAS USER cv=3.61501e11 GM1=0.667
endeos
tracer
  add 100,3.81 fixed=xy
  add 161.985,3.81 fixed=xy
```

```
   add 233.105,3.81 fixed=xy
   add 330.895,3.81 fixed=xy
   add 402.015,3.81 fixed=xy
endtracer
* material insertion inputs
diatom
   package 'hipressure'
     mat 2
     pressure 1.14577e+07
     density 1.85956e-03
    insert box
     p1 = 0,0
     p2 = 122,7.62
    endinsert
   endpackage
   package 'lopressure'
     mat 1
     pressure 7.90466e+05
     density 2.47313e-03
    insert box
     p1 = 122,0
     p2 = 442,7.62
    endi
   endp
enddiatom

edit
   shortt
     tim = 0., dt = 1e-5
```

```
  ends
*
  longt
    tim = 0., dt = 1.0
  endl
  restt
    tim = 0.
    dtf = 5e-5
  endr
*
ende

boundary
  bhydro
    bxbot = 0 , bxtop = 0
    bybot = 0 , bytop = 0
  endhydro
endb
mindt
    time = 0. dt = 1.e-9
endn
```

Appendix B

Mesh Convergence

B.1 SESAME Grid Convergence

SESAME table refinement studied EOS sensitivity to grid spacing in the T, v, P and T, v, e surfaces. In this instance when we say 'grid' we are referring to the spacing of the thermodynamic points and not the spatial mesh. As described in Table 2.1, we used refinement levels to study the relative errors of the shock speeds when using different resolutions of SESAME tables. The configurations run are shown in Table B.1. Absolute relative error was computed using

$$\delta = \frac{|x_1 - x_2|}{0.5(x_1 + x_2)}, \tag{B.1}$$

where x_1 and x_2 are any two variables with the same units. Convergence was assumed if $\delta \leq 1 \times 10^{-3}$. The shock speeds were compared between levels 1 to 2, 2 to 3, and 1 to 3. Figure B.1 shows the relative error between and demonstrates that in all but one case the simulation could be considered converged at level 1 refinement. Each ring of Figure B.1 corresponds to an error magnitude relative to the previous SESAME refinement level. Radial lines in Figure B.1 correspond to a combination of driver and test section pressures listed in Table B.1. Recall that a level 1 refine-

ment corresponded to a $\Delta T = 24\,K$ and $\Delta v = 50\,\frac{cm^3}{g}$. Each subsequent refinement halved the property step size. All simulations in this thesis were run with a level 3 refinement.

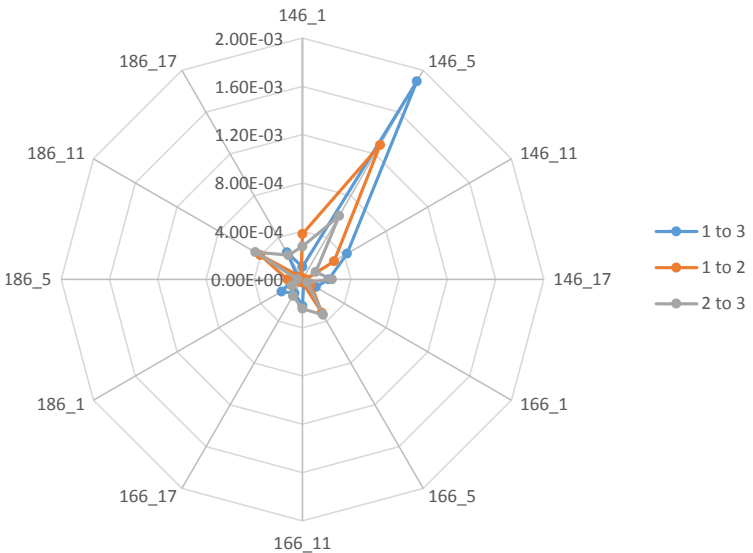

Figure B.1: Shock speed relative error in SESAME convergence

Table B.1: SESAME Convergence Tests

Name	Driver Pressure (psia)	Test Pressure (psia)
146_1	146	1.14
146_5	146	5.70
146_11	146	11.4
146_17	146	17.1
166_1	166	1.14
166_5	166	5.70
166_11	166	11.4
166_17	166	17.1
186_1	186	1.14
186_5	186	5.70
186_11	186	11.4
186_17	186	17.1

B.2 Spatial Mesh Convergence

Spatial refinement levels are described in Table 2.3. Levels 1, 2, 3, and 5 were simulated for 12 different cases. Recall that ascending mesh level denotes a grid refinement of one-half in all directions. The goal was to determine simulation sensitivity to mesh size. CTH uses second-order-accurate methods for advection and mesh remap, although results themselves are not necessarily second-order-accurate since some numerical dissipation is present due to adjustments to the first and second coefficients of viscosity required for numerical stability across the shock [14]. In some sense, the same simulation is not run twice since the value of the viscosities change based on simulation parameters. Relative error between refinement levels is calculated by

$$\varepsilon_{ij} = \frac{f_j - f_i}{f_j}, \tag{B.2}$$

where f_i is the i^{th} level value, f_j is the j^{th} level value, and j must be the finer grid [24]. Values computed using Equation B.2 can be used to estimate the order of accuracy of an algorithm. Order of accuracy is given by

$$\frac{\varepsilon_{12}}{r_{12}^p - 1} = r_{23}^p \left[\frac{\varepsilon_{23}}{r_{23}^p - 1} \right], \tag{B.3}$$

where ε is defined in Equation B.2, r is the rate of mesh refinement (e.g. 2, for halving of the mesh size), ε_{12} is a coarse grid error, and ε_{23} is a fine grid error [24]. Equation B.3 is simple to solve if $r_{12} = r_{23} = r$ and reduces to $p = \ln(\varepsilon_{12}/\varepsilon_{23})/\ln(r)$. Otherwise Equation B.3 is transcendental in p [24]. If f is not monotone with mesh refinement, error may not be positively valued. To avoid imaginary values, the magnitude of the error ratio should be used in such cases. Order of convergence can be used to estimate the value of f^*, assuming a perfect mesh, where $f^* = \lim_{h \to 0} f_i(h)$. Care must be exercised since non-monotone behavior can indicate that something is happening inside the code to prevent convergence with mesh refinement or the

model is constructed incorrectly [24]. We define h to be the step size in the spatial discretization. After running 3 different mesh sizes to calculate p, f^* can be directly calculated by [24]

$$f^* = f_3 + \frac{f_3 - f_2}{r^p - 1}. \tag{B.4}$$

Equation B.4 performs well for both monotone and non-monotone values of f. However if $p \to 0$, the extrapolation to f^* is suspect since the method becomes discontinuous. This is shown in Table B.4 where the $\phi = 25.6$ case extrapolates to a value far away from what is expected. Values in Tables B.2, B.3, and B.4 were used to create Figures B.2, B.3, and B.4 that present error in shock speed, pressure, and temperature relative to f^* plotted as $\ln(|\varepsilon|)$ versus $\ln(\Delta x)$.

A level 5 set of simulations was run since the values in Table B.2 are non-monotonic. The sets of estimated p values were worse than the level 3 case but the shock speed values were very similar to the level 1, 2, and 3 cases. Thus it was determined that the first and second coefficients of viscosity dominate the results and mesh refinement could not reduce error further.

Table B.2: Shock Speed Values

ϕ	f_1 $[m/s]$	f_2 $[m/s]$	f_3 $[m/s]$	f^* $[m/s]$	p	ε_{12}	ε_{23}
128.1	931.730	932.893	932.284	931.611	0.931	1.247e-03	6.540e-04
25.6	601.383	602.298	601.722	600.744	0.667	1.518e-03	9.562e-04
12.8	482.760	483.610	483.330	483.192	1.601	1.759e-03	5.798e-04
8.5	421.521	422.070	421.830	421.644	1.195	1.300e-03	5.680e-04
145.6	959.690	961.936	961.669	961.633	3.073	2.335e-03	2.775e-04
29.1	624.794	626.138	625.785	625.659	1.928	2.146e-03	5.639e-04
14.6	503.293	504.262	504.094	504.059	2.529	1.922e-03	3.329e-04
9.7	440.342	441.097	440.815	440.647	1.421	1.713e-03	6.397e-04
163.2	985.906	988.208	987.556	987.298	1.819	2.329e-03	6.602e-04
32.6	646.261	647.794	647.256	646.964	1.508	2.367e-03	8.321e-04
16.3	522.143	523.222	523.009	522.956	2.341	2.062e-03	4.071e-04
10.9	457.488	458.463	458.123	457.941	1.520	2.127e-03	7.416e-04

Table B.3: Shock Pressure Values

ϕ	f_1 $[psia]$	f_2 $[psia]$	f_3 $[psia]$	f^* $[psia]$	p	ε_{12}	ε_{23}
128.1	28.7196	28.6965	28.6911	28.6895	2.115	8.053e-04	1.859e-04
25.6	58.6819	58.6622	58.6610	58.6609	4.018	3.354e-04	2.071e-05
12.8	74.3954	74.6633	74.7866	74.8914	1.122	3.588e-03	1.649e-03
8.5	83.4709	83.7313	83.8758	84.0554	0.852	3.110e-03	1.723e-03
145.6	30.5587	30.5326	30.5253	30.5226	1.854	8.564e-04	2.369e-04
29.1	63.4878	63.4755	63.4749	63.4748	4.347	1.942e-04	9.540e-06
14.6	81.4129	81.6538	81.6727	81.6743	3.671	2.950e-03	2.315e-04
9.7	91.5456	91.8446	91.9482	92.0030	1.531	3.255e-03	1.127e-03
163.2	32.2523	32.2185	32.2115	32.2097	2.277	1.050e-03	2.166e-04
32.6	67.9913	67.9922	67.9923	67.9923	3.652	1.408e-05	1.120e-06
16.3	88.0072	88.0465	88.0270	88.0076	1.007	4.457e-04	2.217e-04
10.9	99.3308	99.6717	99.8062	99.8935	1.344	3.420e-03	1.347e-03

Table B.4: Shock Temperature Values

ϕ	f_1 $[K]$	f_2 $[K]$	f_3 $[K]$	f^* $[K]$	p	ε_{12}	ε_{23}
128.1	722.6238	717.7034	716.5803	716.2474	2.129	6.856e-03	1.567e-03
25.6	488.7871	486.8125	484.8367	906.3445	-0.007	4.056e-03	4.075e-03
12.8	421.5859	420.0232	419.9085	419.8994	3.768	3.720e-03	2.732e-04
8.5	390.0532	388.7837	388.8209	388.8220	5.094	3.265e-03	9.558e-05
145.6	746.9986	741.8187	740.5133	740.0725	1.986	6.983e-03	1.763e-03
29.1	503.3376	500.9906	498.9173	482.6320	0.173	4.685e-03	4.156e-03
14.6	432.5402	431.2649	430.6129	429.9285	0.966	2.957e-03	1.514e-03
9.7	399.4374	397.8766	397.8284	397.8269	5.018	3.923e-03	1.211e-04
163.2	769.3374	763.9528	762.3900	761.7491	1.782	7.048e-03	2.050e-03
32.6	516.8604	514.2089	512.4115	508.5876	0.556	5.156e-03	3.508e-03
16.3	442.7632	441.6357	440.4817	485.8571	-0.037	2.553e-03	2.620e-03
10.9	408.1788	406.5399	406.5029	406.5020	5.469	4.031e-03	9.099e-05

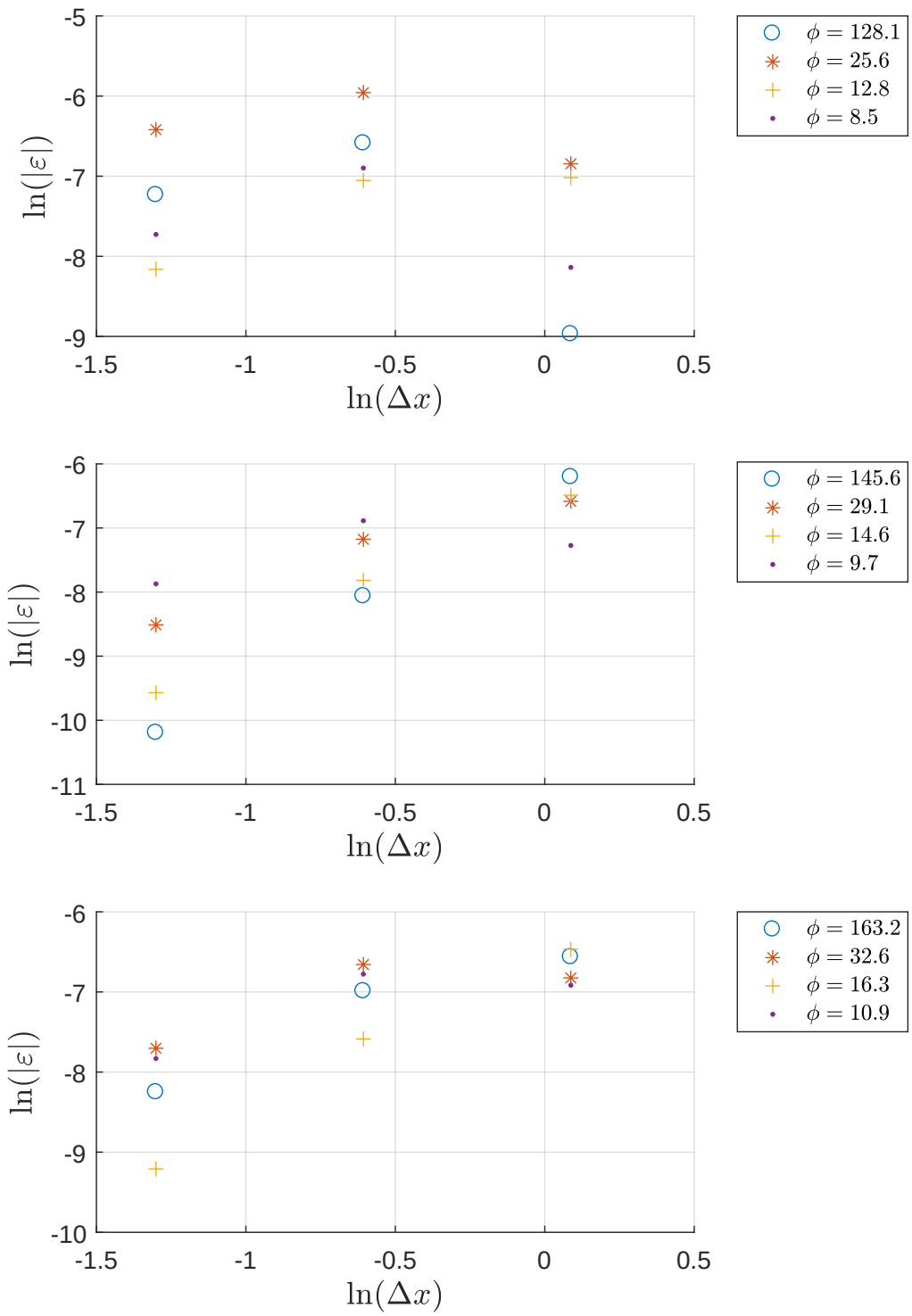

Figure B.2: Shock Speed Logarithmic Error of Mesh Levels 1, 2, and 3

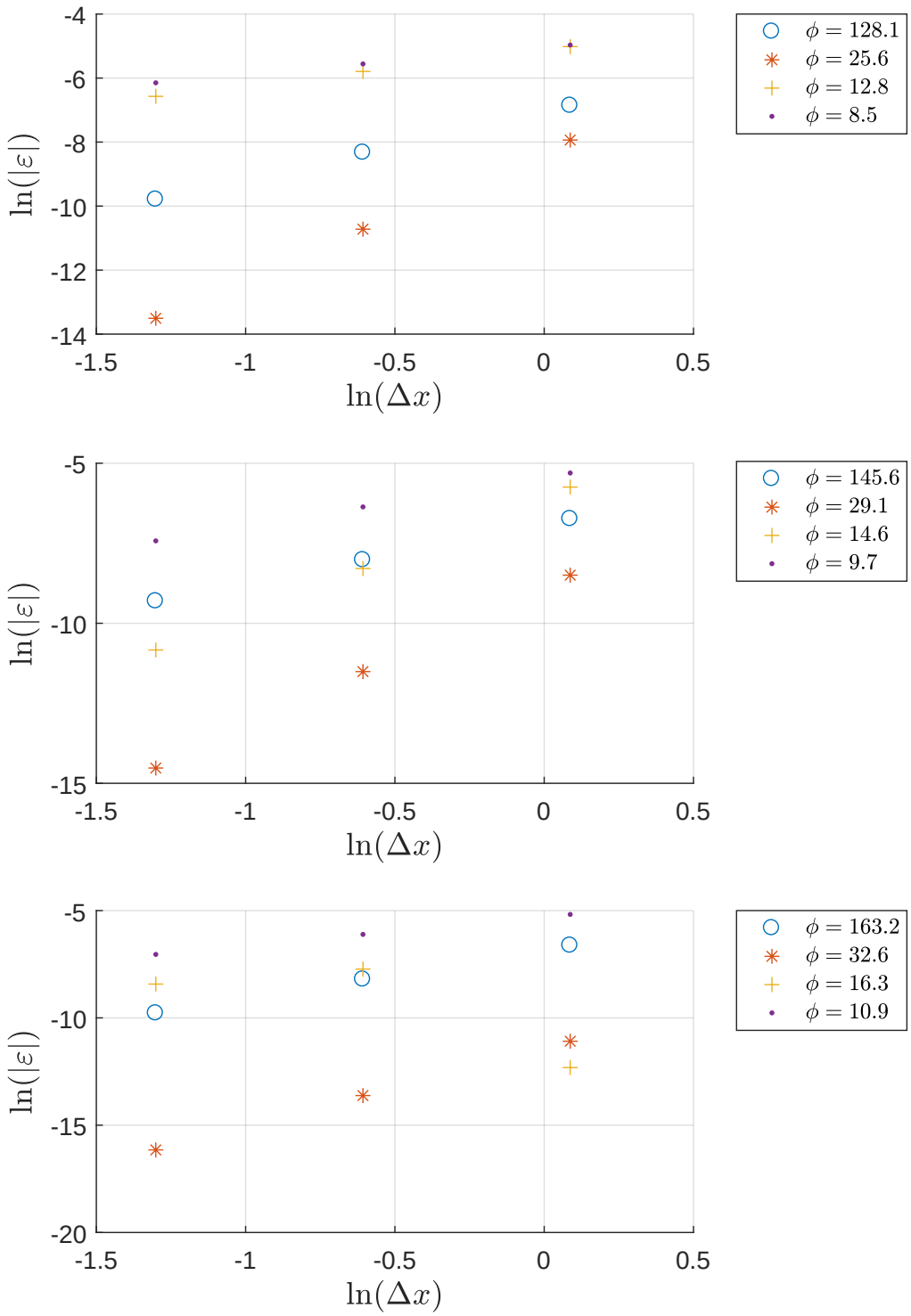

Figure B.3: Shock Pressure Logarithmic Error of Mesh Levels 1, 2, and 3

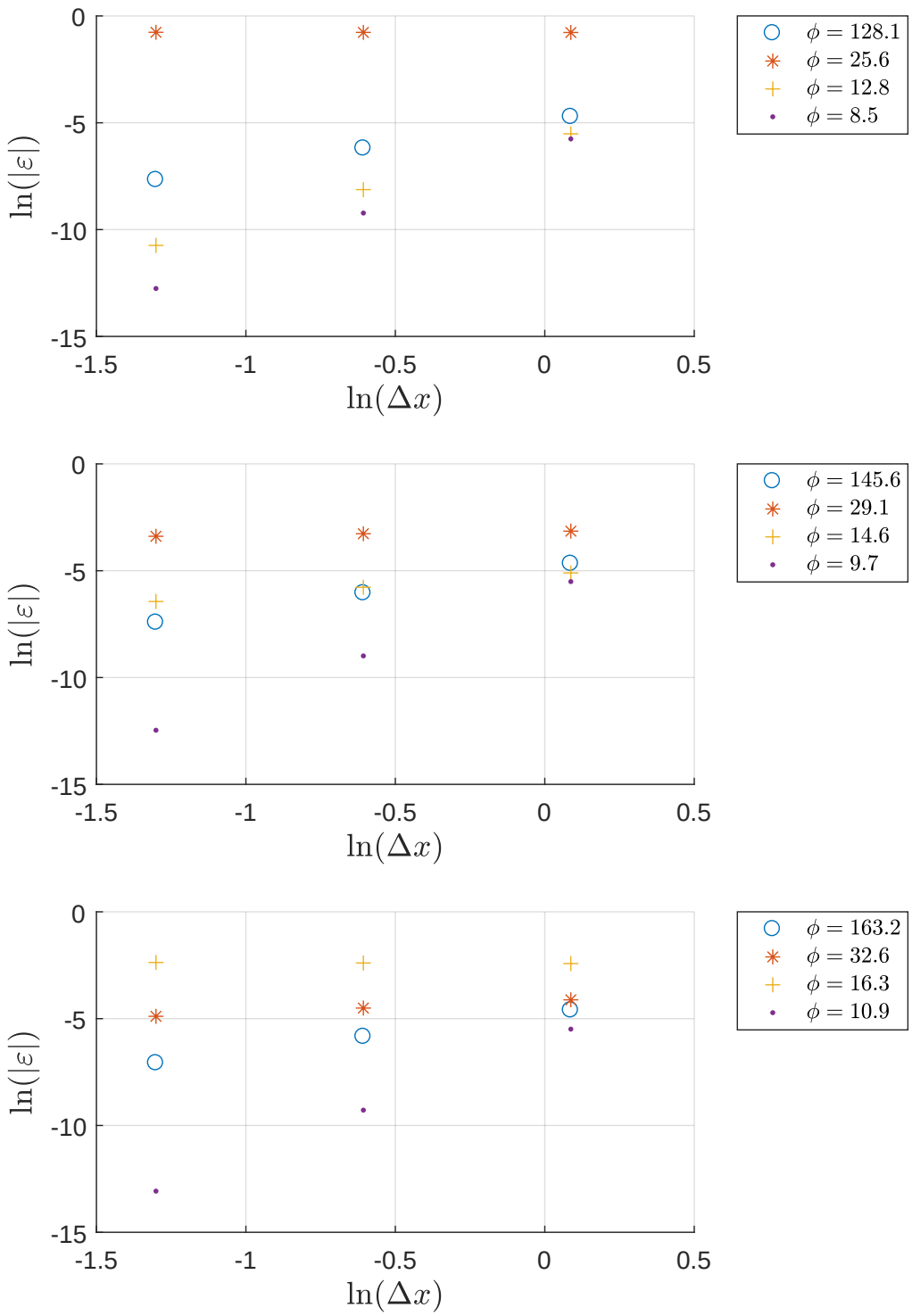

Figure B.4: Shock Temperature Logarithmic Error of Mesh Levels 1, 2, and 3

Appendix C

Algorithms

In order to make the process of computing U_s, P_s, and T_s tractable, MATLAB scripts were used. This appendix briefly outlines how it was done and shows sample calculations.

C.1 Calculating U_s

Computation of U_s depended on an analogue of an x-t diagram. CTH outputs particle velocity at a tracer in the *hscth* file. The script simply looked to see when velocity at the tracer was greater than zero (0) and recorded the time from the *hscth* time history column. This reduces to an overdetermined system since we desire a fit of the form $x = U_s \cdot t + b$ and four tracers were used. Computing the shock speed was a matter of solving

$$\begin{bmatrix} t_1 & 1 \\ t_2 & 1 \\ t_3 & 1 \\ t_4 & 1 \end{bmatrix} \begin{bmatrix} U_s \\ b \end{bmatrix} = \begin{bmatrix} 161.985 \\ 233.105 \\ 330.895 \\ 402.015 \end{bmatrix}, \tag{C.1}$$

where t_i is the shock arrival time in seconds at the i^{th} tracer and the right hand side represents shock tube lengthwise tracer locations in centimeters. The value of b is not used directly in computing U_s, but not forcing the fit to pass through zero improves the quality of the fit. Correlations were checked as a way to see how well the speed was resolved from the data. Every correlation value was unity, indicating expected shock speed behavior.

C.2 Calculating P_s and T_s

When the shock front passes it induces pressure and temperature spikes that can be determined using numerical derivatives. A centered-difference scheme was used at each tracer. The temporal derivative is given by

$$\frac{df}{dt} \approx \frac{f^{i+1} - f^{i-1}}{2\Delta t}, \tag{C.2}$$

where f is the quantity of interest and t is time. The derivative was maximum when the shock passed. Thus, finding the time corresponding to the maximum derivative value allowed the MATLAB script to find the maximum shock pressure and temperature. An example of shock pressure is shown in Figure C.1 where the shock is nice and crisp. Slight amounts of ringing are observed on the expansion at tracers 1 and 2. However, checks were performed by hand to show that the script was not fooled by the presence of slight oscillations. For shock temperature shown in Figure C.2, the temperature spikes due to the shock but then rapidly drops due to the expansion of the gases following the shock. Again, the shock front is sharp and well defined allowing for easy calculation of numerical derivatives to find maximum temperatures.

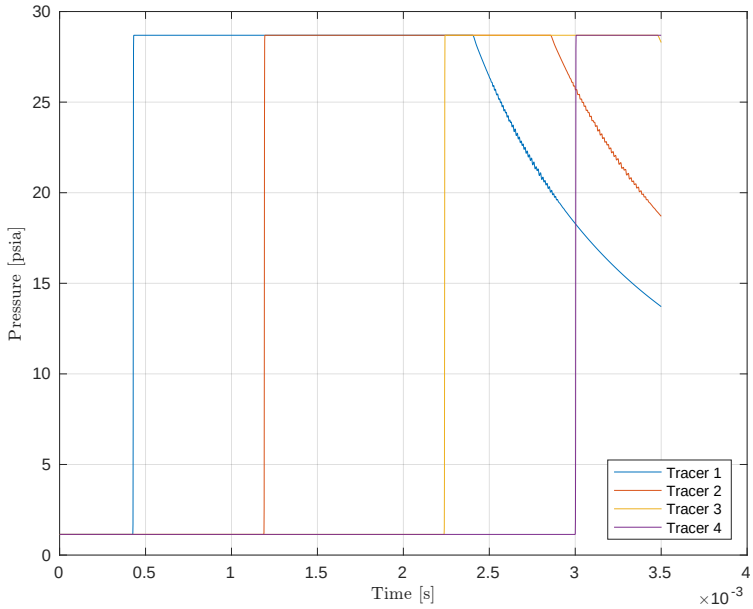

Figure C.1: Tracer Pressure History for $\phi = 128.1$

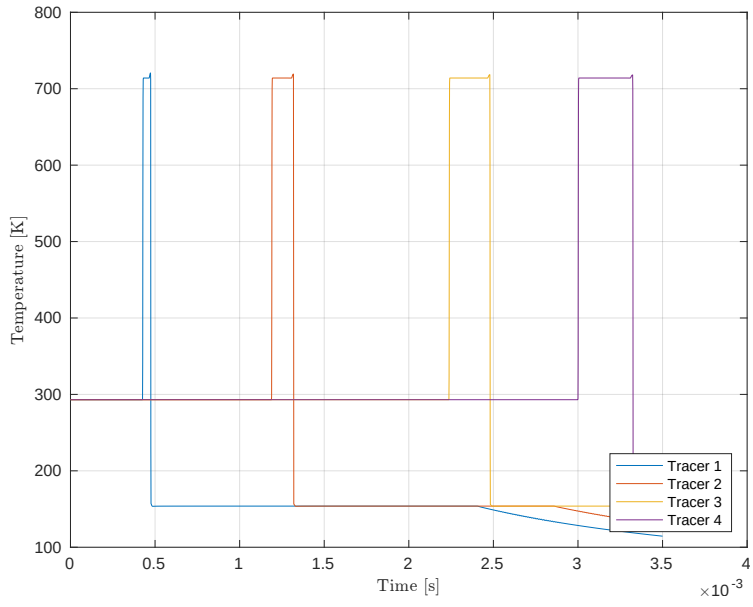

Figure C.2: Tracer Temperature History for $\phi = 128.1$

References

[1] I. Trueba Monje and J. H. Yoo, "Investigation of Dalton's Law and Amagat's Law for Mixtures Using Shock Wave Propagation," *AIAA Region IV Student Conference Paper*, April 2016.

[2] G. D. Wyss and K. H. Jorgensen, "A Users's Guide to LHS: Sandia's Latin Hypercube Sampling Software," Software Documentation SAND98-0210, Sandia National Laboratories, 1998.

[3] K. W. Woo and S. I. Yeo, "Dalton's Law vs. Amagat's Law for the Mixture of Real Gases," *The SNU Journal of Education Research*, vol. 5, pp. 127–134, 1995.

[4] G. J. Van Wylen and R. E. Sonntag, *Fundamentals of Classical Thermodynamics*. Hoboken, NJ: Wiley, 2nd ed., 1973. pp. 405-420,431-476.

[5] D. Li, V. Sankaran, J. W. Lindau, and C. L. Merkle, "A Unified Computational Formulation for Multi-Component and Multi-Phase Flows," *AIAA Paper 2005-1391*, January 2005.

[6] C. L. Merkle, J. Y. Sullivan, P. E. O. Buelow, and V. Sankaran, "Computation of Flows with Arbitrary Equations of State," *AIAA Journal*, vol. 36, pp. 515–521, April 1998.

[7] P. S. Tow, "Evidence of Validity of Amagat's Law in Determining Compressibility Factors for Gaseous Mixtures under Low and Moderate Pressures," *Journal of Physical Chemistry*, vol. 68, pp. 2021–2023, July 1964.

[8] G. A. Bird, "The Structure of Normal Shock Waves in a Binary Gas Mixture," *Journal of Fluid Mechanics*, vol. 31, no. 4, pp. 657–668, 1968.

[9] F. S. Sherman, "Shock-wave Structure in Binary Mixtures of Chemically Inert Perfect Gases," *Journal of Fluid Mechanics*, vol. 8, no. 3, pp. 465–480, 1960.

[10] J. A. Beattie, "The Computation of the Thermodynamic Properties of Real Gases and Mixtures of Real Gases," in *Symposium on Thermodyanmics and Molecular Structure of Solutions*, September 1948.

[11] J. A. Beattie, "A Rational Basis for the Thermodynamic Treatment of Real Gases and Mixtures of Real Gases," *Physical Review*, vol. 36, no. 240, pp. 132–145, 1930.

[12] M. Hobbs, M. R. Baer, and B. C. McGee, "JCZS: An Intermolecular Potential Database for Performing Accurate Detonation and Expansion Calculations," *Propellants, Explosives, Pyrotechnics*, vol. 24, pp. 269–279, 1999.

[13] H. B. Callen, *Thermodynamics and an Introduction to Thermostatistics*. New York, NY: Wiley, 2nd ed., 1985. pp. 35-39.

[14] J. M. McGlaun, S. L. Thompson, and M. G. Elrick, "CTH: A Three-Dimensional Shock Wave Physics Code," *International Journal of Impact Engineering*, vol. 10, pp. 351–360, 1990.

[15] E. Clapeyron, "Mèmoire sur la puissance de la chaleur," *Journal de l'Ècole Polytechnique (in French)*, vol. XIV, pp. 153–190, 1834.

[16] R. D. Cowan and W. Fickett, "Calculation of the Detonation Properties of Solid Explosives with the Kistiakowski-Wilson Equation of State," *The Journal of Chemical Physics*, vol. 24, no. 5, pp. 932–939, 1956.

[17] S. Itoh, H. Hamashima, K. Murata, and Y. Kato, "Determination of JWL Parameters from Underwater Explosion Test," *in 12th International Detonation Symposium*, vol. 281, 2002.

[18] E. Lee, M. Finger, and W. Collins, "JWL Equation of State Coefficients for High Explosives," Technical Report UCID-16189, Lawrence Livermore Laboratory, 1973.

[19] M. Cowperthwaite and W. Zwisler, "The JCZ Equations of State for Detonation Products and Their Incorporation in the TIGER Code," *Sixth Symposium (International) on Detonation*, no. ACR-221, pp. 162–172, 1976.

[20] B. McGee, M. Hobbs, and M. Baer, "Exponential 6 Parametrization for the JCZ3-EOS," Sandia Report SAND98-1191, Sandia National Laboratories, 1998.

[21] C. L. Mader, "Detonation Properties of Condensed Explosives Computed Using the Becker-Kistiakowsky-Wilson Equation of State," Technical Report LA-2900, Los Alamos Scientific Laboratory, 1963.

[22] E. Lee, H. Hornig, and J. Kury, "Adiabatic Expansion of High Explosive Detonation Products," Technical Report UCRL-50422, Lawrence Radiation Laboratory, 1968.

[23] S. Lyon and J. Johnson, "SESAME: The Los Alamos National Laboratory Equation of State Database," Technical Report LA-UR-92-3407, Los Alamos National Laboratory, 1992.

[24] P. J. Roache, *Verification and Validation in Computational Science and Engineering*. Albuquerque, NM: Hermosa Publishers, 2009. pp. 109-131.

[25] R. D. Zucker and O. Biblarz, *Fundamentals of Gas Dynamics*. Hoboken, NJ: Wiley, 2nd ed., 2002. pp. 147-158.

[26] E. N. Harstad, "CTH Shock Physics." `http://www.sandia.gov/CTH/`. Accessed: 15 March 2017.

[27] N. Tsoulfanidis and S. Landsberger, *Measurement and Detection of Radiation*. Boca Raton, FL: CRC Press, 3rd ed., 2011. pp. 17-58.

[28] J. M. Bland and D. G. Altman, "Measurement Error," *BMJ*, vol. 312, no. 7047, p. 1654, 1996.

[29] M. D. Mckay, R. J. Beckman, and W. J. Conover, "A Comparison of Three Methods for Selecting Values of Input Variables in the Analysis of Output from a Computer Code," *Technometrics*, vol. 42, pp. 55–61, 2000.

[30] M. S. Weitzman, "Measures of Overlap of Income Distributions of White and Negro Families in the United States," *U.S. Government Printing Office*, vol. 22, pp. 1–37, 1970.

[31] T. E. Clemmons and E. L. Bradley, "A Nonparametric Measure of the Overlapping Coefficient," *Computational Statistics and Data Analysis*, vol. 34, pp. 51–61, 2000.